University of Nebraska - Lincoln
DigitalCommons@University of Nebraska - Lincoln

USGS Staff -- Published Research | US Geological Survey

9-27-2022

Neural net detection of seismic features related to gas hydrates and free gas accumulations on the northern U.S. Atlantic margin

Urmi Majumdar

Nathaniel C. Miller

Carolyn D. Ruppel

Follow this and additional works at: https://digitalcommons.unl.edu/usgsstaffpub

 Part of the Geology Commons, Oceanography and Atmospheric Sciences and Meteorology Commons, Other Earth Sciences Commons, and the Other Environmental Sciences Commons

This Article is brought to you for free and open access by the US Geological Survey at DigitalCommons@University of Nebraska - Lincoln. It has been accepted for inclusion in USGS Staff -- Published Research by an authorized administrator of DigitalCommons@University of Nebraska - Lincoln.

U.S. government works are not subject to copyright.

Neural net detection of seismic features related to gas hydrates and free gas accumulations on the northern U.S. Atlantic margin

Urmi Majumdar[1], Nathaniel C. Miller[2], and Carolyn D. Ruppel[2]

Abstract

Bottom-simulating reflections (BSRs) that sometimes mark the base of the gas hydrate stability zone in marine sediments are often identified based on the reverse polarity reflections that cut across stratigraphic layering in seismic amplitude data. On the northern U.S. Atlantic margin (USAM) between Cape Hatteras and Hudson Canyon, legacy seismic data have revealed pronounced BSRs south of the deepwater extension of Hudson Canyon and more subtle ones from offshore Delaware south to Cape Hatteras, where the reflections sometimes follow stratigraphic layering. Using high-resolution seismic data acquired during the 2018 Mid-Atlantic Resource Imaging Experiment and a supervised neural net, we identify seismic features associated with gas hydrates and/or the top of gas between Hudson Canyon and Cape Hatteras. Using seismic attributes especially sensitive to the presence of gas, we train a neural network algorithm on seismic data from an area with strong BSRs and then apply the model to the rest of the data set. The results indicate that gas hydrate and/or shallow free gas are significantly more widespread on the northern part of the USAM than previously known. Seismic indicators of gas extend landward from the 2000 m isobath to the upper continental slope in sectors with (offshore Virginia) and, to a lesser extent, without (offshore New Jersey) pervasive upper slope methane seeps. Higher sand content and intermediate sediment thickness, factors related to the container size and gas charge in a petroleum systems framework, are associated with more robust gas indicators.

Introduction

The distribution of gas hydrate along the U.S. Atlantic margin (USAM) remains poorly constrained decades after Markl et al. (1970) first identified bottom-simulating reflections (BSRs) on the Blake Ridge offshore South Carolina and Tucholke et al. (1977) imaged these features within the Mid-Atlantic Bight (MAB) offshore New Jersey and Delaware. On the Blake Ridge, which was one of the first major marine provinces recognized as hosting widespread gas hydrates, an Ocean Drilling Program expedition (ODP Leg 164) and a series of major seismic programs refined BSR maps and the details of gas hydrate distributions and saturations (e.g., Holbrook et al., 1996; Paull et al., 1996; Collett and Ladd, 2000; Hornbach et al., 2008). In contrast, few studies have explicitly focused on gas hydrate distributions on the USAM north of Cape Hatteras, even though a recent analysis of individual seismic lines found BSRs in many locations (Ruppel et al., 2022) and more than 550 methane seeps have been discovered on the upper slope in this sector (Skarke et al., 2014). In fact, the quantitative hydrate assessment conducted by the Bureau of Ocean and Energy Management (BOEM) predicts more gas-in-place in hydrates on the northern part of the USAM than in the area encompassing Blake Ridge (BOEM, 2012) and approximately the same amount of gas-in-place in hydrates along the entire USAM as in the northern Gulf of Mexico.

BSRs are negative polarity reflections (indicative of a change from higher to lower seismic wavespeeds with increasing depth in the sediments) that often are interpreted as marking the base of hydrate-bearing sediments (HBS) and/or the top of vapor phase gas in the pore spaces of underlying sediments (e.g., Holbrook et al., 1996). Vapor phase gas often is referred to as the free gas, as it will be in the remainder of this paper. BSRs sometimes cut across stratigraphic layering and may have morphology resembling a muted form of seafloor bathymetry owing to their coincidence with thermodynamic (pressure-temperature) conditions at the hydrate phase transition. HBS exist in many places with no associated BSR (e.g., Paull et al., 1996), but the presence of a BSR often implies that HBS exist somewhere within the overlying sedimentary section (Majumdar et al., 2016). Thus, the extent of BSRs can provide valuable insights into the minimal geographic distribution of gas hydrate.

[1]Woods Hole Oceanographic Institution, Woods Hole, Massachusetts, USA and U.S. Geological Survey, Woods Hole, Massachusetts, USA. E-mail: urmi.geology@gmail.com.

[2]U.S. Geological Survey, Woods Hole, Massachusetts, USA. E-mail: ncmiller@usgs.gov (corresponding author); cruppel@usgs.gov.

Manuscript received by the Editor 23 December 2021; revised manuscript received 2 May 2022; published ahead of production 1 August 2022; published online 27 September 2022. This paper appears in *Interpretation*, Vol. 10, No. 4 (November 2022); p. T785–T806, 13 FIGS., 2 TABLES. http://dx.doi.org/10.1190/INT-2021-0248.1. © 2022 Society of Exploration Geophysicists and American Association of Petroleum Geologists

BSRs are traditionally identified based on the visual interpretation of amplitude sections in air-gun seismic data, which have the appropriate frequency content to highlight BSRs. In locations such as the MAB, BSRs can be discontinuous or parallel to stratigraphic layering (Majumdar et al., 2019; Ruppel et al., 2019), characteristics that render visual identification difficult and reduce confidence that the appropriate reflections have been chosen. BSRs are used as an indicator not only for the existence of gas hydrate or underlying free gas accumulations but also as a proxy for thermal conditions in the shallow sedimentary section. The utility of BSRs beyond gas hydrate studies lends additional importance to the appropriate identification of these features.

To overcome the challenges associated with visually identifying BSRs in the MAB portion of the northern USAM, we applied a supervised neural network (NN) model to a modern high-resolution multichannel seismic (MCS) data set acquired by the U.S. Geological Survey (USGS) in 2018. In this paper, we describe the analytical approach, the results obtained for the MAB, the physical meaning of the seismic features assigned high confidence by the NN model, and the implications for gas hydrate distributions and the petroleum system on the USAM.

Study area

The focus area for this study is the MAB, stretching from offshore Long Island, New York, on the north to roughly Cape Hatteras, North Carolina, on the south (Figure 1). This part of the USAM rifted from northwestern Africa starting in late Triassic time, and its evolution, morphology, subsidence, and sedimentation patterns have been influenced by relict structures from Paleozoic orogenies, interaction with the Central Atlantic large igneous province, the development and filling of onshore (e.g., Newark and Culpeper) and offshore (e.g., Baltimore Canyon Trough) rift basins, and other large-scale processes (e.g., Manspeizer, 1988; Marzoli et al., 1999; Thomas, 2006). The continental shelf of the contemporary MAB extends from the shoreline to waters at a depth of approximately 100–125 m and widens from approximately 40 km at Cape Hatteras to more than 130 km offshore New Jersey. A steep continental slope reaches 2000 m below sea level (mbsl) within 25–35 km seaward of the shelf break, which is breached by six major canyons (Hudson, Wilmington, Baltimore, Washington, Norfolk, and Keller) from the north to south. Farther seaward, the outer continental rise has a gently sloping morphology and is mantled by thick Paleogene and Neogene sediments and sediment drift deposits (e.g., Twichell et al., 2009).

During Pleistocene time, most sediment was delivered to the continental shelf and upper slope of the MAB by the Hudson and James River and through Delaware and Chesapeake Bays. At the Last Glacial Maximum, thick sediment piles had accumulated on upper slopes and in shelf-edge deltas along parts of the MAB, particularly across the head of Hudson Canyon, between Baltimore and Washington Canyons, and south of Norfolk Canyon. Destabilization of these shelf-edge deltas (e.g., Hill et al., 2004; Dixon et al., 2012) contributed to submarine slope failures that mar nearly the entire upper slope, contributing to mass transport deposits (MTDs) that today blanket parts of the lower slope and continental rise. Inactive pockmarks (Brothers et al., 2014), widespread methane seepage (e.g., Skarke et al., 2014),

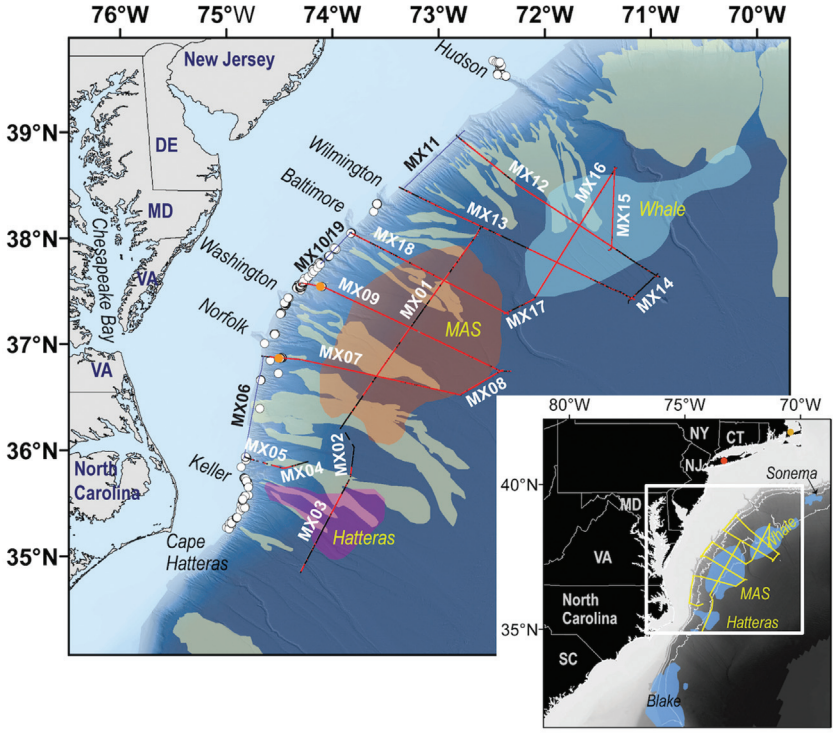

Figure 1. Map of the study area showing MATRIX (MX) seismic lines relative to the three MAB gas hydrate prospects (Whale, MAS, and Hatteras) identified by Frye et al. (2013). The green polygons extending from the upper slope to deep water are slope failures (Twichell et al., 2009). The red points along the MATRIX lines mark CMPs where the neural net analysis produced confidence values greater than 0.95. The white circles show locations of methane seeps (Skarke et al., 2014; Baldwin et al., 2020b). The orange circles on MX07 and MX09 correspond to the Norfolk seeps and Chincoteague seeps, respectively (e.g., Ruppel et al., 2022). Six major shelf-break canyons (Hudson through Keller) within the study area are labeled on the shelf. Accomac and Phoenix Canyons, whose drainages cross some of the seismic lines, lie south of Baltimore Canyon. Inset: Location map for this part of the USAM, with the white box surrounding area shown in a larger map. Blake and Sonema (southern New England margin; Ruppel et al., 2022) hydrate prospects identified by Frye et al. (2013) are shown in blue shading, along with the MAB prospects. The red and orange circles mark Long Island and Cape Cod, respectively.

and pervasive gas charging of shallow sediments (Hill et al., 2004; Ruppel et al., 2022) characterize the contemporary outermost shelf and upper continental slope.

A recent study documents BSRs along the USAM from the South Atlantic Bight to southern New England in seismic data collected before 2018 but does not provide a new map of the areal distribution of BSRs (Ruppel et al., 2022). Here, we adopt the gas hydrate prospects defined by BOEM (BOEM, 2012; Frye et al., 2013) based on the analysis of BSRs in legacy seismic data as a starting point for our study of MAB gas hydrate distributions in the high-resolution MCS data acquired in 2018. From north to south, the BOEM analysis identified three primary gas hydrate prospects, which we call (1) the Whale Prospect, (2) the Mid-Atlantic States (MAS) Prospect, and (3) the Hatteras Prospect.

1) The Whale Prospect (Shedd and Hutchinson, 2006; Ruppel et al., 2022) is a 12,000 km^2 area south of the deepwater extension of Hudson Canyon and coincident with the Chesapeake Drift. Prominent BSRs cut across stratigraphy at approximately 3000 mbsl in legacy data, and seismic reflection data acquired in 2014 (Arsenault et al., 2017) also image a strong BSR in the Whale Prospect (Ruppel et al., 2022). Frye et al. (2013) identify the Whale Prospect as a high certainty gas hydrate area.
2) The MAS Prospect lies at approximately 2000–3500 mbsl and stretches roughly from the Delaware River to the outlet of Chesapeake Bay. BOEM (Frye et al., 2013) assigns intermediate probability to this gas hydrate prospect, which has an area of approximately 21,000 km^2. Where BSRs can be recognized in legacy USGS seismic data in this prospect, they often run parallel to stratigraphic layering or are coincident with unconformities (e.g., Majumdar et al., 2019; Ruppel et al., 2022).
3) At approximately 4500 km^2, the Hatteras Prospect is the smallest of the northern USAM gas hydrate prospects identified by BOEM (2012). The area with identified BSRs extends from shallower than 2000 to more than 3500 mbsl, with the shallowest part being a narrow (approximately 20 km wide) neck that extends up Keller Canyon following one of the USGS legacy seismic lines. Similar to the MAS Prospect, the Hatteras Prospect was identified at an intermediate confidence level (Frye et al., 2013), and the BSRs are difficult to discern in seismic amplitude data (Majumdar et al., 2019; Ruppel et al., 2019).

Data

This study relies on the continental slope portion of approximately 2000 line kilometers of 2D MCS data acquired during the 2018 Mid-Atlantic Resource Imaging Experiment (MATRIX) (Ruppel et al., 2019), which was led by the USGS with additional support from the U.S. Department of Energy (DOE) and BOEM. MATRIX acquired data between Cape Hatteras and the deepwater extension of Hudson Canyon at water depths of approximately 125 to almost 4000 m, mostly along margin-parallel strike lines and margin-perpendicular dip lines. The placement of seismic lines was designed to sample landward and through deepwater prospects identified by BOEM (Frye et al., 2013) as having moderate to high probability of BSRs based on an analysis of legacy USGS seismic data acquired with lower source frequency and at lower temporal and spatial sampling rates than the MATRIX data.

The seismic source for the MATRIX survey was two or four 105/105 in^3 Sercel generator-injector (GI) guns towed in pairs from the *R/V Hugh R. Sharp* in August 2018. The air guns were run exclusively in GI mode yielding maximum air-gun volume of 420 in^3 (four air guns). Shots were spaced at 25–35 m or at time intervals roughly corresponding to this spatial interval and were recorded on a 700–1200 m long digital streamer having 112–160 channels with 3.125 and 6.25 m group spacing. Streamer positions were determined by depth loggers along the streamer's length and a GPS receiver mounted on a tail buoy. Record lengths were 4–10 s, with sampling intervals of 0.5–1 ms. Complete information about data acquisition and processing is available from Baldwin et al. (2020a), which also supplies the raw and processed MCS data. Additional data associated with MATRIX have been released by Baldwin et al. (2020b, 2021).

Processing of the raw MCS data included corrections for 3D source and receiver geometry; common-midpoint (CMP) binning along 2D crooked lines; frequency-wavenumber and band-pass filtering; wavelet extraction, deterministic deconvolution, and zero phasing; and normal moveout correction, stacking, and poststack phase-shift time migration (Baldwin et al., 2020a). For the water depths that are the focus of this study, normal moveout along the streamer is minimal, and a 1D velocity profile hung from the seafloor produces clear imaging in the upper 1–2 s of sediments.

For the analysis undertaken here, we use the post-stack time migration (post-STM) version of the MATRIX data set as the starting point and focus only on analysis of the subset of MATRIX data that was not collected along strike lines at the shelf break. Those lines are too shallow (<200 mbsl) for hydrate-related features to be present. We do include in the analysis the entirety of the MATRIX dip lines that image from the shelf-break down the upper continental slope, even including data at water depths nominally too shallow (less than approximately 550 mbsl; Brothers et al., 2014) for hydrate-related features. The total number of CMPs for the data set used in this analysis is approximately 567,000.

Methods

This section outlines the supervised NN methodology applied to identify features associated with gas hydrate and/or free gas in the high-resolution MCS data.

Neural network

We use the NN module in *OpendTect* software (dGB Earth Sciences, 2021) to develop a supervised multiattribute pattern recognition model for seismic features that

share characteristics with BSRs. The workflow follows the outline of Meldahl et al. (2001) and involves selecting a suite of seismic attributes that can identify seismic objects related to the gas hydrates and/or free gas; defining a training data set that includes similar sample sizes from locations with and without the targeted seismic objects and extracting the selected set of seismic attributes from the two classes; and then training the NN. The trained NN is then applied to the entire data set to identify all the locations with seismic objects that share the base of gas hydrate/top of gas characteristics with objects in the training data set and to assign a confidence value to these objects.

The supervised pattern recognition module of *OpendTect* NNs plugin (dGB Earth Sciences, 2021) uses a feed-forward multilayer perceptron network (Hush and Horne, 1993) that maps an input layer to an output (i.e., classification) layer via a set of hidden layers (Figure 2). A back-propagation algorithm iteratively adjusts weights that minimize the classification error between predicted outputs and ground truth values in the training data set for a given input-output pair. The weights determine the relative importance of input attributes for a specific output.

The general NN workflow used here has been applied to seismic interpretation problems such as the identification of fluid migration pathways and faults (Heggland et al., 1999; Meldahl et al., 1999, 2001; Ligtenberg, 2005; Kluesner and Brothers, 2016), reservoir characterization (Walls et al., 1999; Tonn, 2002; Russell, 2004), geohazard delineation (Aminzadeh et al., 2002; Heggland, 2004), seismic facies analysis (West et al., 2002; Wrona et al., 2018), and karst detection and imaging (Ebuna et al, 2018). Machine-learning and deep-learning approaches also have been previously used for gas hydrate studies in other geographic settings. For example, Jeong et al. (2014) apply an NN to estimate gas hydrate saturation in the Ulleung Basin from seismic attributes and well-log data. Bedle (2019) and Chenin and Bedle (2020) combine the seismic multiattribute approach with rock-physics modeling to identify weak BSR-like seismic reflections in the Pegasus Basin, New Zealand.

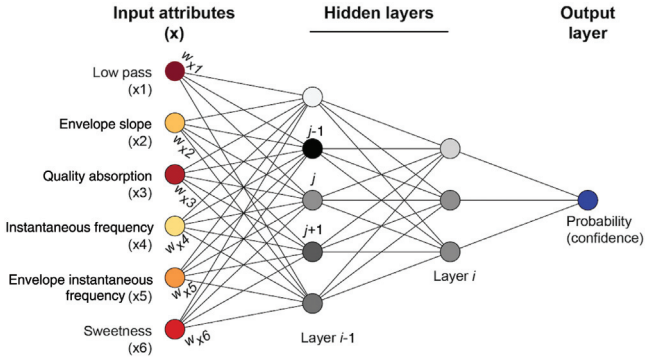

Figure 2. Schematic of the multilayer perceptron NN used to identify SIG. Nodes are shown as circles with network connections marked by lines. The relative influence of each input layer seismic attribute (x_1–x_6) on the classification is indicated by the white-yellow-orange-red color scale, with red indicating higher weight (w). The relative influence of hidden layer nodes is qualitatively indicated by gray scaling. The actual neural net has many more hidden layers than the two shown here. The network connection from the ith node in layer $i-1$ to the jth node in layer i is weighted by w_{ij}. The output layer is the probability (confidence) that a location in the seismic image has the same characteristics as the attributes associated with the BSR or top of gas in the training data set.

Seismic attributes

To train the NN, we extract a variety of seismic attributes (e.g., Chopra and Marfurt, 2005, 2008) from the post-STM data. In some studies, prestack attributes such as amplitude-variation-with-angle/offset also have been found to be diagnostic of the base of hydrates (Bedle, 2019; Chenin and Bedle, 2020). However, the MATRIX data were collected with a relatively short streamer (<1200 m), and the data lack the offsets needed to determine prestack attributes at the water depths common in the study area.

The post-STM-based seismic attributes that we chose for training the NN detect changes in seismic properties related to the presence of gas hydrate and/or free gas in marine sediments (e.g., Satyavani et al., 2008; Hien et al., 2010; Kim et al., 2014; Bedle, 2019). These attributes, which are summarized in Figure 3, rely on amplitude and frequency characteristics. As noted previously, BSRs approximate the base of thermodynamic stability for gas hydrates in sediments, but the negative polarity of these features arises from the contrast in wavespeeds across these reflections: Underlying sediments typically contain at least a small amount of free gas, leading to lower wavespeeds than those above BSRs, where gas hydrate may or may not be present. However, gas hydrate provinces may have features other than BSRs that are associated with similar amplitude and/or frequency changes. For example, free gas confined by lithologic or structural traps leads to anelastic attenuation and suppression of higher frequencies (e.g., Wood et al., 2000), characteristics that may cause these features to have seismic attributes similar to BSRs. Distinguishing between free gas associated with a BSR versus other features is difficult when relying on poststack seismic attributes alone, especially where BSRs are roughly parallel to stratigraphy, as they are in parts of the MAB. Because the attributes that we use in the NN are more generally sensitive to the top of gas than the presence of hydrate, we refer to features identified by the NN framework as seismic indicators of gas (SIG). Here, we briefly describe each of the seismic attributes used in the NN framework.

The *low-pass* attribute x_1 (Figure 2) is a <50 Hz low-pass filter applied to post-STM amplitude data. The MATRIX data were processed up to approximately 450 Hz and image gas charging in fine-scale structures. The low-pass filter tunes these fine-scale features to a single reflection, which is more reliably detected by the NN. The low-pass data retain polarity, so this attribute is sensitive to the negative impedance contrast associated with the top of the sediments hosting free gas.

We calculated several other attributes based on the complex analytic signal. For an input amplitude trace $s(t)$, the analytic is

$$A(t) = s(t) + ig(t) = \mathrm{Env}(t)\exp[i\Phi(t)], \qquad (1)$$

where $g(t)$ is the Hilbert transform of $s(t)$, $\mathrm{Env}(t) = \sqrt{s(t)^2 + g(t)^2}$ is the envelope, and $\Phi(t) = \tan^{-1}(g(t)/s(t))$ is the phase angle.

The *delta envelope slope* attribute x_2 is the difference in the first derivative of envelope averaged in windows above and below each sample, which is a small time section (e.g., 200 ms) of seismic data along a single trace. Differencing of adjacent windows can be written compactly as a convolution:

$$x_2 = F^{-1}\left[F\left(\frac{d\mathrm{Env}(t)}{dt}\right)\Psi^*\right], \qquad (2)$$

where F and F^{-1} denote the forward and inverse Fourier transforms, respectively, and Ψ is the Fourier transform of a negative Harr-like wavelet, which, for a window length of n samples, is $-1/n$ for the first n samples and $1/n$ for the next n samples. The asterisk denotes the complex conjugate. Envelope, like amplitude, is sensitive to the impedance contrast at the top of gas. Envelope data do not contain any polarity information but are proportional to reflection energy, which helps the NN distinguish the transition from lower-amplitude sedimentary reflectors to higher-amplitude reflections at the top of gas-charged sediments. The first derivative of the envelope helps the NN detect the change from low-to-high versus high-to-low-reflection energy, which avoids duplicate detections on both sides of the signal associated with the top of gas-charged sediments. This change is highlighted by taking the difference of time windowed averages above and below each sample.

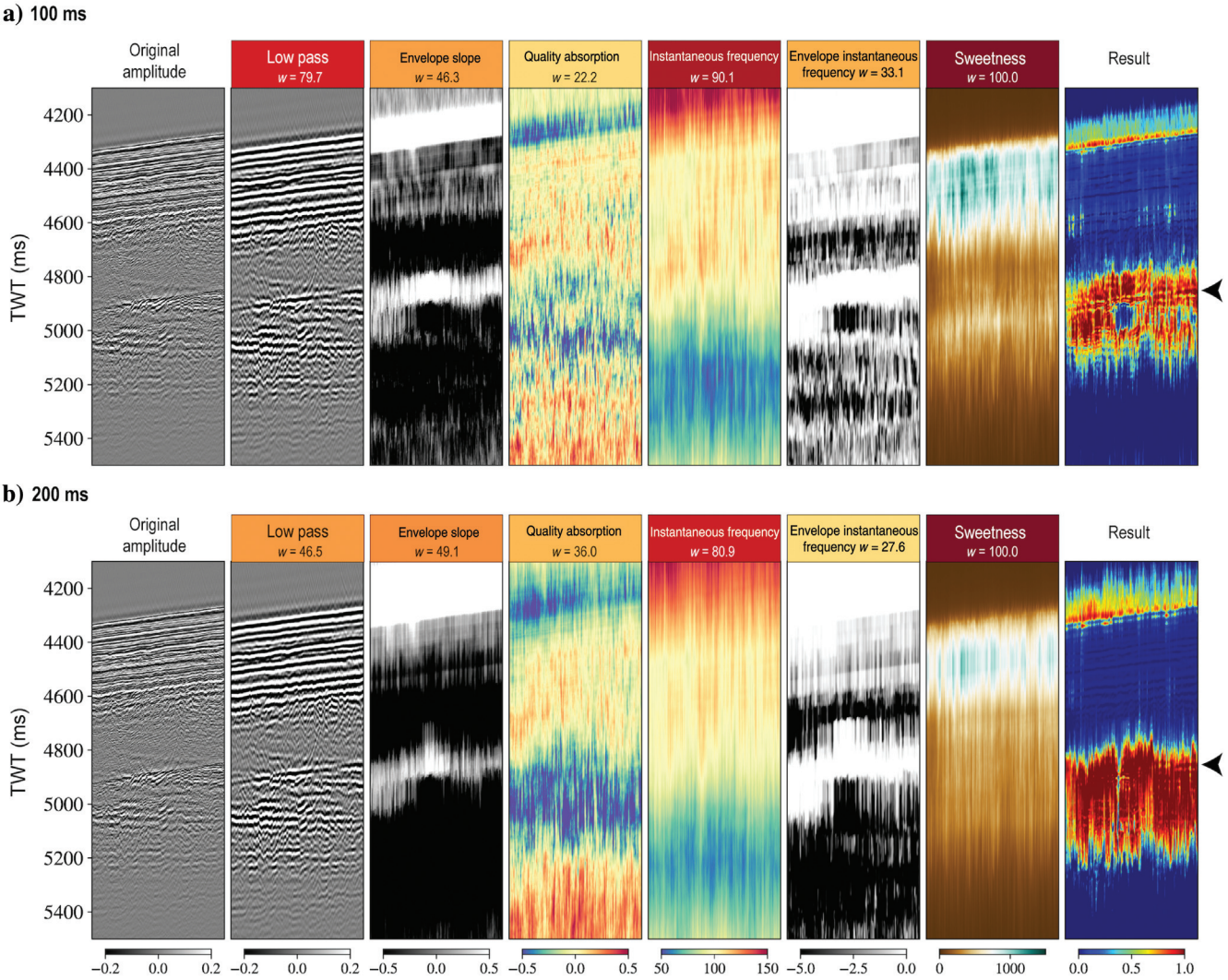

Figure 3. Examples of data, attributes, and NN output. Data are from a section of MX12 (Whale Prospect) showing a prominent BSR crosscutting stratigraphy. Far left panel shows the original amplitude sections from the seismic data. Panels with colored headers are attributes used in the NN, and the w values are weights assigned by the NN. The NN result is shown in the far right panel. The arrow marks the actual BSR location. Attributes and NN output are shown for (a) 100 ms and (b) 200 ms window sizes.

The *delta quality absorption factor* attribute x_3 is a measure of attenuation. Here, "quality absorption" is defined as the area under the power spectra beyond the dominant frequency, weighted by frequency. This attribute is determined by first calculating the short-time power spectra in windows around each sample:

$$A(t,\omega) = \mathcal{F}^{-1}[|S(\omega)|^2 W(\omega)^*], \tag{3}$$

where $S(\omega)$ and $W(\omega)$ are the Fourier transforms of the amplitude trace $s(t)$ and a Gaussian window function w, respectively. Dominant frequency $\omega_0(t)$ is defined as the frequency with the maximum power at each time:

$$\omega_0(t) = \arg\max_{\omega} A(t,\omega). \tag{4}$$

Then, a quality absorption factor $Q_a(t)$ is calculated from each short-time power spectra by integrating the values beyond ω_0:

$$Q_a(t) = \sum_{\omega=\omega_0}^{\pi/dt} \omega A(t,\omega), \tag{5}$$

where the upper bound on the summation is the Nyquist angular frequency. Finally, averages of adjacent windows are differenced using

$$x_3 = \mathcal{F}^{-1}[\mathcal{F}[Q_a(t)]\Psi^*]. \tag{6}$$

For simplicity, we set the width of the short-time power spectra window W to match the width of Ψ. In the presence of free gas in the sediments, high frequencies are attenuated, causing the area beyond the dominant frequency to decrease. Differencing adjacent windows highlights this change.

Attenuation caused by gas or fluids below HBSs is expected to produce a low-frequency anomaly. To detect this change, we calculate a *delta instantaneous frequency* attribute x_4, which is the difference in instantaneous frequency between windows above and below each sample. Ordinary instantaneous frequency can be calculated from phase angle as

$$f(t) = \frac{1}{2\pi}\frac{d\Phi(t)}{dt}. \tag{7}$$

As described previously, differencing is accomplished by convolution:

$$x_4 = \mathcal{F}^{-1}[\mathcal{F}[f(t)]\Psi^*]. \tag{8}$$

We also calculate the *envelope weighted instantaneous frequency* attribute x_5, which scales instantaneous frequency by energy in the seismic trace and reduces spikes and rapidly changing variations by applying a Gaussian smoothing operator:

$$x_5 = \mathcal{F}^{-1}[\mathcal{F}[\mathrm{Env}(t) f(t)]W^*]. \tag{9}$$

The *sweetness* attribute x_6 is the ratio of envelope to the square root of instantaneous frequency (Radovich and Oliveros, 1998), which we also smooth:

$$x_6 = \mathcal{F}^{-1}\left[\mathcal{F}\left[\frac{\mathrm{Env}(t)}{\sqrt{f(t)}}\right]W^*\right]. \tag{10}$$

Sweetness is often used to detect hydrocarbons (Hart, 2008). Along a BSR or other reflection at the top of gas-charged sediment, a higher value of envelope and a lower value of instantaneous frequency produce high sweetness values. In contrast, a decrease in instantaneous frequency and amplitude, as is the case with attenuation from spherical spreading, produces lower values of sweetness. Similarly, a high-amplitude reflection with high instantaneous frequency also produces a low sweetness value, which may be indicative of a lithologic contrast without associated pore fluids or gas (e.g., a dry structural trap).

Attributes used in the NN inherently include time averaging, which causes a loss of resolution and also improves spatial continuity and pattern recognition. The delta envelope slope, delta instantaneous frequency, and delta quality absorption factor attributes are all calculated by taking differences of windowed averages from above and below each sample. Sweetness and envelope weighted instantaneous frequency are calculated with moving windows. For each NN model, we set these window sizes to a constant length. We evaluated the NN performance for a range of window sizes (50–500 ms) for time averaging to identify the optimal window that balanced generalization and resolution of the results. Small time windows produced higher resolution results (e.g., closely matching the position of the BSR where it could be visually identified), but the resulting model was less applicable to the data set as a whole.

Model performance was generally worse for window sizes larger than 200 ms or smaller than 100 ms. The performance of the NN based on these two different attribute extraction window sizes is shown in Figure 2 and summarized in Table 1. To visualize the metrics, a confusion matrix (Table 2) can be constructed that compares the true and the model predicted outputs, with the rows and columns, respectively, representing the true and predicted classes. Based on these analyses, we chose 200 ms as the optimal window size.

Training data set

To build a learning data set for training the NN, we first visually identified BSRs within the Whale Prospect (Shedd and Hutchinson, 2006) using MATRIX data. In the center of Whale Prospect, BSRs are continuous and parallel to stratigraphy but can still be identified based on their strong amplitude and reverse polarity. On the seaward side of the mounded sediments that make up much of the Whale Prospect, the BSRs cut across stratigraphy and their character depends on the seismic frequency. At frequencies above approximately 50 Hz, the BSRs appear as discontinuous high-amplitude reflections where stratigraphic units inferred to be charged with free gas intersect the base of gas hydrate stability (BGHS), as shown in Figure 3. At frequencies lower than approximately 50 Hz,

these individual reflections appear continuous. For NN training, we picked BSRs as continuous horizons based on the lower-frequency data.

During the supervised learning, the NN assigns different weights to the training seismic attributes. The performance of the NN continues to improve as the algorithm iteratively changes the assigned weights (Figure 4) until learning is complete. One challenge associated with training the NN using seismic attributes associated with strong BSRs in the Whale Prospect is that the same attributes may not be as useful in areas with more subtle SIGs. For example, the envelope attribute was assigned high importance in the Whale Prospect training data set during our initial applications of the NN. However, much smaller amplitude anomalies are associated with SIGs in other parts of the MAB, meaning that the envelope attribute is not as useful for delineating these features outside of the Whale Prospect. To mute the influence of raw amplitude anomalies in NN learning, we combined amplitude and frequency anomalies by including the instantaneous frequency weighted by envelope.

Validation

The *OpendTect* NNs tool (dGB Earth Sciences, 2021) uses a single hold-out cross validation method (Berrar, 2019) in which a small fraction (10% in our model) of the training data set is randomly sampled into a validation (or test) subset (Hush and Horne, 1993). Training is stopped when the percent misclassification and the test normalized root-mean-squared (rms) error between the NN predictions and true values start to increase after decreasing for most of the model run. The best NN model is associated with the smallest normalized rms error and smallest misclassification, as shown in Figure 4.

Choosing the highest SIG probability at each CMP

Application of the NN produces a probability or confidence value for each sample in the seismic images. Values greater than 1.0 are possible and, indeed, expected in evaluating some of the seismic lines. The first reason that probabilities may exceed 1.0 is mathematical and dependent on the extrapolation function used in the OpenDTect NN toolbox (dGB Earth Sciences, 2021). The second reason is physical and related to the differences between the training data set and the rest of the data to which the NN is applied. For example, the NN for this study was trained using seismic attributes from places with and without a BSR in the Whale Prospect. When seismic data elsewhere in the MATRIX data set had attributes that were even more indicative of the desired seismic features than those

Table 1. Quantitative assessment of NN model performance on a test data set for 200 and 100 ms attribute extraction windows.

Error statistics	200 ms window	100 ms window
Normalized rms	0.35	0.5
Percent misclassification	5	8
Precision[3]	0.82	0.74
Recall[4]	0.97	0.92
$F1$ score[5]	0.89	0.82

[3]Precision is the ratio of true positives to the sum of true and false positives from the NNs confusion matrix.
[4]Recall is the ratio of true positives to the sum of true positives and false negatives from the NNs confusion matrix.
[5]The $F1$ score is the harmonic mean of precision and recall.

Table 2. Confusion matrices for 200 ms attribute extraction window and 100 ms attribute extraction window.

200 ms window	Predicted BSR (%)	Predicted non-BSR (%)
True BSR	19.98	0.54
True non-BSR	4.34	75.14
100 ms window	Predicted BSR (%)	Predicted non-BSR (%)
True BSR	18.82	1.63
True non-BSR	6.42	73.12

Values are given in percentages.

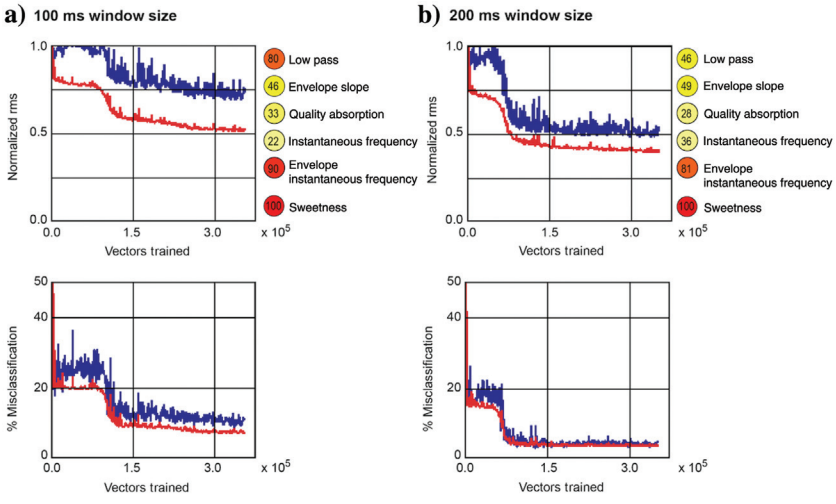

Figure 4. The neural net performance graphs for the (a) 100 ms and (b) 200 ms time windows as generated by OpendTect. The top panel in each part of the figure shows the change in normalized rms misfit for the test data (blue) and the training data (red) for an increasing number of neural net iterations on the x-axis. The bottom panel shows the misclassification for the test and training data, and the colored circles to the right indicate the relative weights (the yellow represents low and the red represents high) given to each of the input seismic attributes.

in the training data set, a confidence value higher than 1.0 was produced.

We used the confidence values produced by application of the NN to generate confidence images for each CMP along each 2D seismic line used in this data set (Figures 5, 6, 7, 8, and 9). The NN result for each CMP has two measures of uncertainty, which are, respectively, associated with the two-way traveltime (TWT) and the confidence value itself. For the analyses in this paper, we chose the SIG depth at the TWT corresponding to the highest confidence value along each CMP. The TWT for the highest confidence values is bracketed on the top at 100 ms below the seafloor and on the bottom by a theoretical deepest viable BGHS calculated for unrealistically cold bottom water temperature and a low, 30°C/km geothermal gradient using a mathematical fit (Ruppel and Waite, 2020) to the Sloan and Koh (2007) hydrate stability determinations and assuming hydrostatic pressure within seafloor sediments and 100% methane as the hydrate former in equilibrium with standard seawater. The conversion from depth to TWT for this bracketing was done assuming a constant velocity of 1514 m/s below the seafloor. For the shallow part of the sedimentary section, using this constant velocity ensures that the bound will be at a larger TWT than if we adopted a more realistic velocity model derived from the long-offset USGS Atlantic margin data set described by Arsenault et al. (2017).

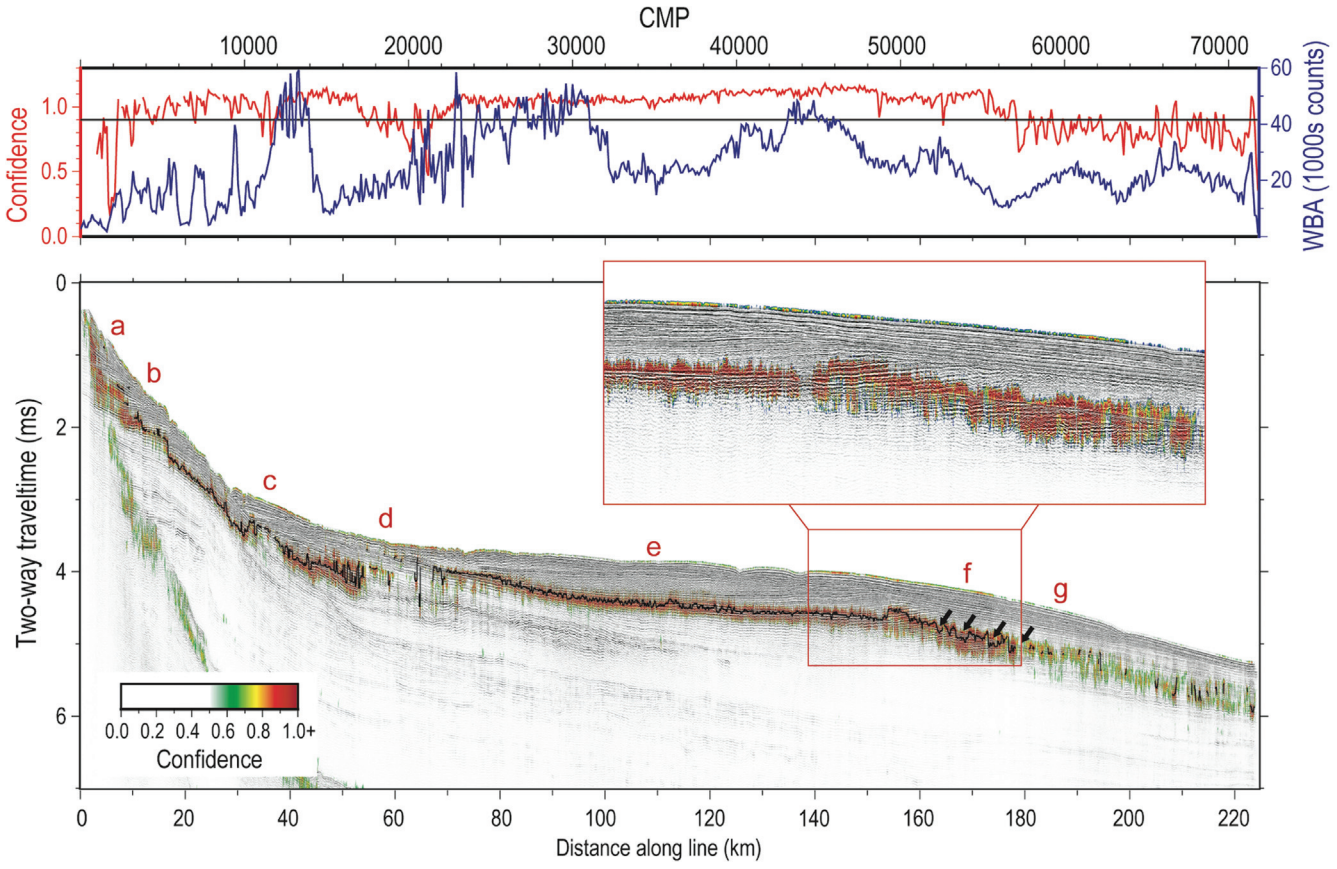

Figure 5. Example results from neural net analysis of the MATRIX data are shown at the bottom, here overlaid on seismic amplitude data along dip line MX12. The highest confidence picks at each CMP (red) and the WBA (blue; in thousands of counts), a proxy for signal quality, are shown on the graph above the seismic image. The color scale for plotting confidence results means that only values greater than 0.5 are visible, and the seafloor has been muted for plotting. The blue dots and lines show training picks for the NN. The black line on the seismic image is a smoothed curve connecting the highest confidence (>0.95) for adjacent CMPs to highlight the best picks and how they sometimes connect laterally to trace out a reflection or other feature. (a) Patchy high confidence values on the upper slope. Some high confidence locations were not marked as SIGs because the values do not exceed the 0.95 threshold. (b) Section with patchy high confidence and significant vertical oscillation of the highest confidence picks, possibly within a slump deposit. Note the high confidence values identified by the NN despite some of the lowest signal quality (based on the WBA proxy — blue curve in the top graph) along this line. (c) Discontinuous high confidence values crosscutting stratigraphy. (d) More than 20 km wide section with no high confidence zone and a few high probability picks at dramatically different depths at approximately 65 km. (e) Laterally continuous high confidence arrayed just below a strong BSR identified in the amplitude data. Despite oscillations in the signal quality (WBA proxy), the confidence remains high throughout this section. (f) Lateral transition to discontinuous, shoaling, and poorly defined high confidence values at a location with BSRs (shown by arrows and a red line) that are easily identified visually from the amplitude data. Inset highlights the details of these features. (g) Lower confidence zone that roughly matches a BSR on the seaward side of the mounded sediments and coincident with an area of lower signal quality as measured by the WBA.

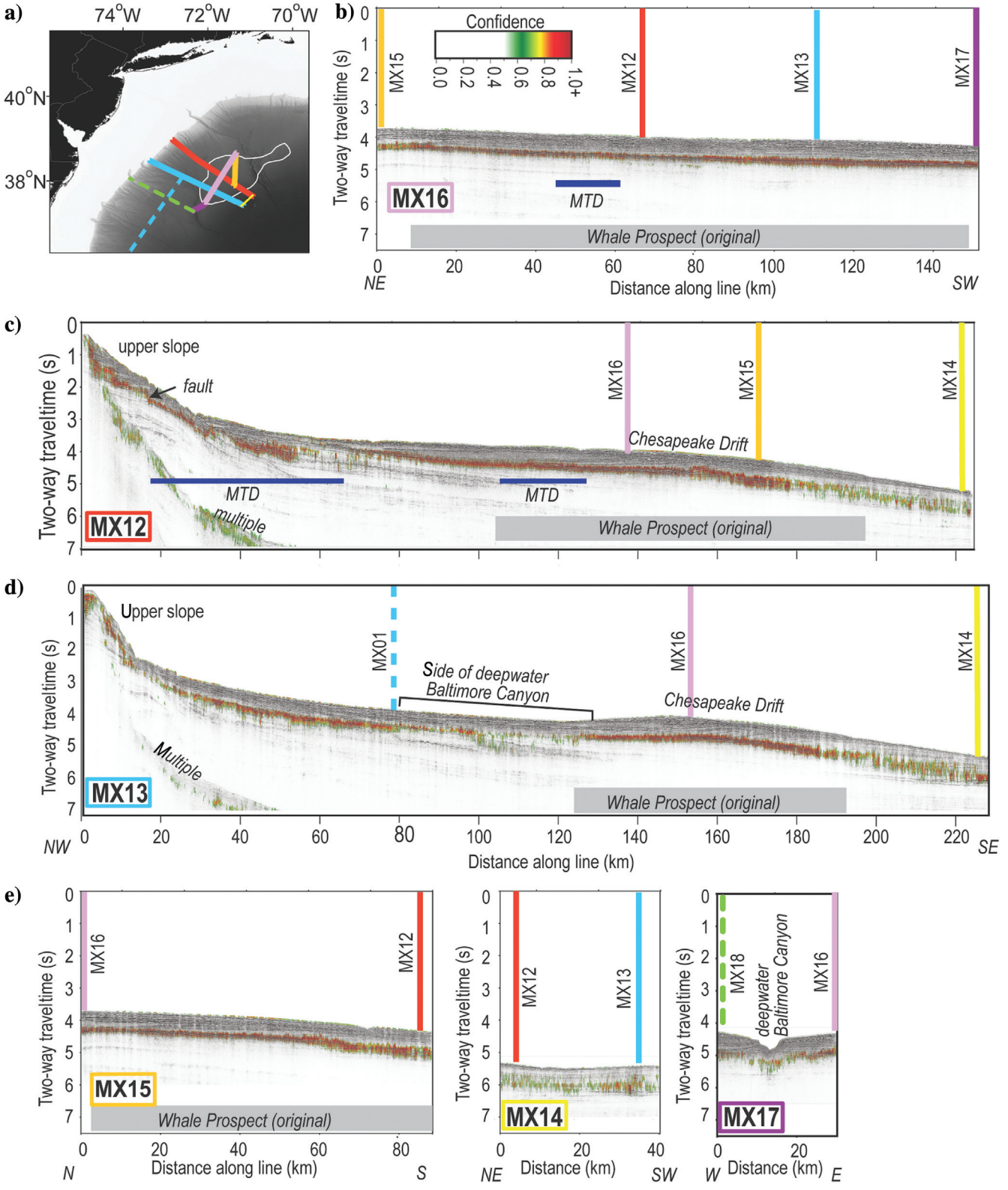

Figure 6. Composite seismic images and neural net results (shown as confidence overlaid on the seismic amplitude data) for the area of the Whale Prospect. (a) Map showing the locations of seismic lines in this figure with the outline of the Whale Prospect in white. Colors correspond to the seismic lines and the tie lines (vertical lines) on each panel of this figure. MX18 (dashed green) and MX01 (dashed blue) are associated with the MAS Prospect and are shown in Figure 7. (b) Strike line MX16, which images through the entire Whale Prospect. The blue line marks where the line crosses an MTD from the slope failure map of Twichell et al. (2009). The confidence color scale is the same for all parts of the figure. The gray box indicates the part of the line coincident with the Whale Prospect as mapped by Shedd and Hutchinson (2006). (c) Dip line MX12. (d) Dip line MX13. (e) MX15, which connects MX16 and MX14; MX14, a strike line seaward of the originally mapped Whale Prospect; and MX17, a line that connects MX16 and MAS Prospect dip line MX18.

Some features identified as SIGs using this approach could be false positives because some of the frequency and impedance changes associated with SIGs also are characteristic of the seafloor, sharp lithologic changes, and other sedimentary features. Conversely, along at least one line, BSRs are clearly visible on the seismic amplitude data but not identified by the NN (false negative; see the "Discussion" section). After choosing the SIG for each CMP at its corresponding TWT based on the confidence threshold, we then connected SIGs at adjacent CMPs. The highest confidence values at adjacent CMPs may be associated with TWTs that differ significantly, imparting an oscillating quality to the high confidence zone along a seismic line. Figure 5 shows an example of the effects of applying a median filter to smooth confidence results that exceeded 0.95 across CMPs on each 2D seismic line. These smoothed confidence values and the corresponding TWT values were used in the calculations described in the "Discussion" section. Figure 5 also plots water bottom amplitude (WBA) as a proxy for signal quality at each trace. The units are given as raw counts, which are related to the pressure digitized by each hydrophone, with no correction for the instrument response.

Results

The overall character of the NN results is demonstrated by the annotated segment of line MX12 in Figure 5, which shows the processed MCS data overlaid by confidence values calculated with the NN and also the smoothed final picks for the SIG for each CMP. Figure 5

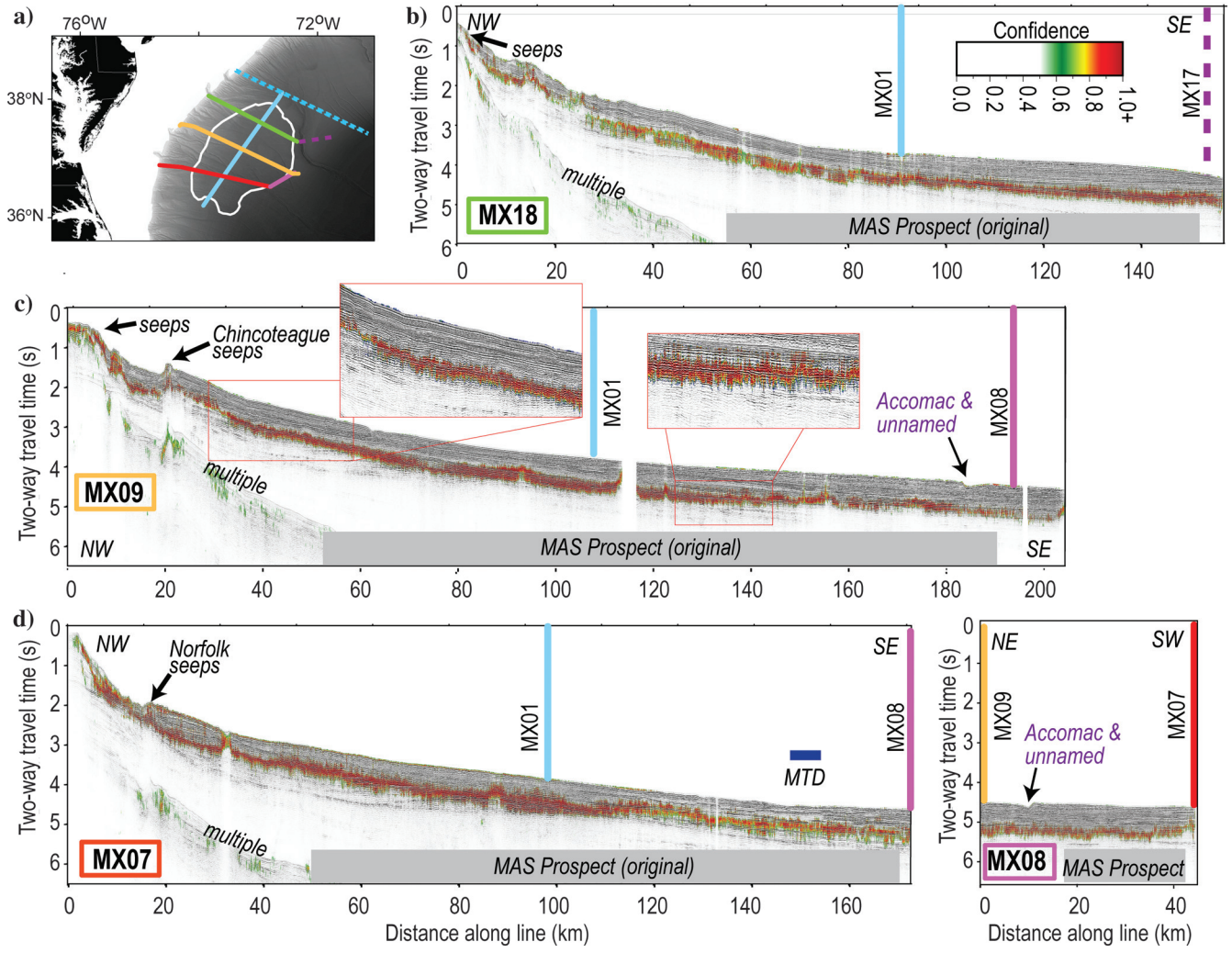

Figure 7. Composite seismic images and neural net results (shown as confidence overlaid on the seismic amplitude data) for the area of the MAS Prospect. (a) Map showing the locations of seismic lines in this figure with the outline of the MAS Prospect in white. Colors correspond to the seismic lines and the tie lines (vertical lines) on each panel of this figure. MX17 (dashed purple) and MX13 (dashed blue; Figure 8) are associated with the Whale Prospect (Figure 6). (b) Dip line MX18. The confidence color scale is the same for all parts of the figure. The gray box indicates the part of the line coincident with the MAS Prospect as mapped by Frye et al. (2013). (c) Dip line MX09, which crosses the Chincoteague seep field (Ruppel et al., 2022). Insets show the detail of two locations along this line. Purple labeling refers to a deepwater drainage that connects to major canyons on the upper slope. (d) Dip line MX07, which crosses the Norfolk seep field, and short line MX08, a short strike line on the seaward side of the MAS Prospect. The blue line on the MX07 image marks a crossing of a MTD from Twichell et al. (2009).

highlights the lateral variability in the vertical position of the SIG and the lack of an identifiable SIG for many CMP based on the application of the NN and the criterion that we impose on the confidence values (>0.95). Figure 5 also shows a comparison of SIG picks to the position of a prominent, visually identified BSR, with the high confidence zone determined by the NN lying just below the BSR in this case.

In this section, we review the results of the NN analysis for the MATRIX lines within and near the three major MAB prospects identified by BOEM (2012): Whale Prospect (lines MX12–MX17), MAS Prospect (lines MX01, MX07–MX09, and MX18), and Hatteras Prospect (lines MX02–MX05). As we examine the character of the SIGs, we also identify features such as faults, which can facilitate gas migration, and seafloor seeps, which are a manifestation of gas migration. We also evaluate laterally discontinuous or absent SIGs and note where the seismic lines cross deepwater canyon drainages or MTDs that can disrupt sediment thickness or composition, potentially leading to changes in the depth of the BGHS (e.g., Ruppel and Waite, 2020).

Whale Prospect area

Although the NN was trained using BSRs that we visually identified within the Whale Prospect, we subsequently applied the NN to all MCS data on lines MX12–MX17, which sample through and around the Whale Prospect (Shedd and Hutchinson, 2006; BOEM, 2012; Ruppel et al., 2022). The NN analysis produces high confidence values coincident with strong, visually identified BSRs within and near the Whale Prospect at approximately 135–170 and 130–180 km along dip lines MX12 and MX13, respectively (Figure 6). High confidence also emerges along the entirety of strike line MX16 and connecting line MX15 and along part of MX17.

The results of the NN analysis support refinements to the mapped extent of the Whale Prospect. As defined by Shedd and Hutchinson (2006) based on BSR mapping, the landward boundary of the prospect approximately coincides with the landward end of the deepwater high confidence zone along MX13 at approximately 125 km. For MX12, the high confidence zone continues landward approximately 35 km beyond the mapped edge (approximately 100 km distance along MX12) of the Whale Prospect. Along MX12, this high confidence zone is continuous with the zone that tracks the BSR through the Whale Prospect itself. However, the zone shoals landward despite the nearly level seafloor and follows stratigraphic layering between approximately 65 and 90 km. As explored next, this shoaling portion of the high confidence zone landward of the mapped Whale Prospect may mark an SIG associated with the top of trapped gas, instead of the BGHS.

On the seaward side of the Whale Prospect, the ends of MX12 (beyond approximately 180 km) and MX13 (beyond approximately 185 km) have sparser distributions of CMPs with confidence exceeding 0.95. The high confidence zones still map out a laterally continuous and relatively coherent SIG that is close to a visually discernible BSR. MX14, which is a short strike line connecting MX12 and MX13, is an example of a line that has a clear BSR where the NN results do not yield strong evidence for SIGs. In this case, the combination of profound water depth (deepest for MATRIX at approximately 4000 mbsl) and relatively small air-gun volume

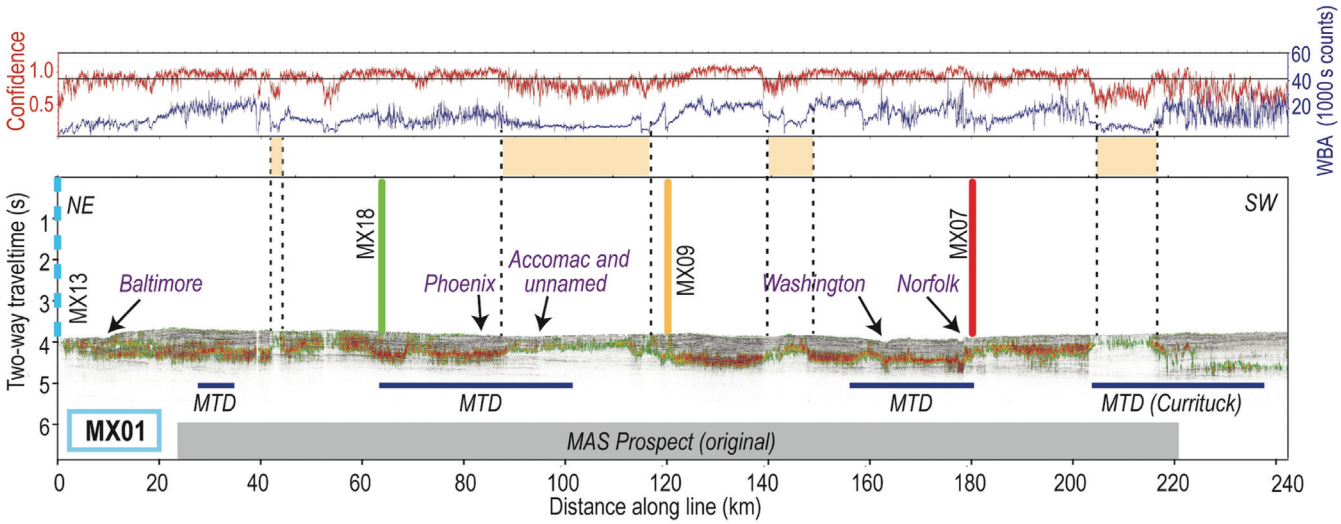

Figure 8. The bottom panel shows the seismic amplitude image for strike line MX01 through the MAS Prospect overlaid with the confidence results from application of the neural net. The position of MX01 and the tied seismic lines (colored vertical lines), along with the scale for the confidence results, are shown in Figure 7. The purple labels show deepwater drainages connected to major and minor shelf-breaking canyons, and the blue lines are MTDs from Twichell et al. (2009). The gray box shows the part of the line that intersects the MAS Prospect as originally mapped by Frye et al. (2013). The top graph shows the maximum confidence along the line at each CMP and the corresponding WBA (in units of thousands of counts), which is a proxy for signal quality. Orange boxes and associated vertical dashed lines link intervals of low signal quality with the corresponding parts of the seismic image and superposed confidence results.

(two or four 105/105 in^3 GI guns) produce a lower quality seismic signal that leads to lower confidence values when the NN algorithm is applied. The discontinuous/low-probability SIGs at the distal ends of MX12 and MX13 and along MX14 also may in part reflect a different geometric relationship between stratigraphy and the BGHS in this area, where the mounded contourite sediments of the Chesapeake Drift dip seaward.

The NN results along strike line MX16 and connecting lines MX15 and MX17, which are approximately strike lines as well, indicate that the northeastern boundary of the main part of the Whale Prospect probably lies at least approximately 10 km beyond its mapped position. On the southwestern side, the high confidence zones at the end of MX16 and continuing into the adjacent part of MX17 show that the Whale Prospect probably extends at least approximately 10 km farther toward the deepwater drainage that can be traced back to Baltimore Canyon. However, the high confidence zone disappears across this submarine canyon on MX17, just as the high confidence zone is absent along MX13 where it sideswipes this drainage at 80–120 km along the line. The Baltimore Canyon drainage could have a different lithology or missing gas charge, or the lack of high confidence within the drainage could reflect its position at the southwestern edge of the Chesapeake Drift, where sediments thin.

Along MX12 and MX13, the upper slope has high confidence zones that are laterally discontinuous with high-probability zones identified seaward of the toe of the slope. The high confidence upper slope zones also are more diffuse and have less of the appearance of an interface than comparable zones in deeper water. The upper slope high confidence zones on these lines shoal landward, as would be expected if the NN is detecting the BGHS, and they follow the stratigraphy for short disjointed segments along MX12 but are less coherent on MX13. At some upper slope locations along MX12 (e.g., approximately 11 and 18 km), discontinuities in the high confidence zones coincide with faults that disrupt the near-seafloor sediments, lending credence to the idea that the identified SIGs may trace gas trapped by specific strata.

MAS Prospect area

Dip lines MX18, MX09, and MX07 traverse the MAS deepwater gas hydrate prospect identified by BOEM (Frye et al., 2013) and image the area landward to the shelf break (Figure 7). High confidence picks roughly coincide with bright reflections that are subparallel to bedding in the deepwater sections of MX18 (90–160 km), MX09 (70–180 km), and MX07 (70–110 km). Landward of these sections, the high confidence zones crosscut stratigraphy at a shallow angle and generally shoal, while remaining roughly parallel to the seafloor. The bright reflections that overlap with the high confidence picks on the MAS dip lines are not laterally continuous within each seismic section, and the lower resolution of the NN results relative to the seismic amplitude images makes correlating the high confidence zones with specific strong reflections challenging.

The upper slope sections of the MAS MATRIX dip lines constrain the subseafloor structure on the part of the northern USAM where more than 250 methane seeps have been discovered (Skarke et al., 2014). Most of these seeps are on the uppermost slope between 200 and 600 mbsl but some emit methane from the seafloor at depths well within the gas hydrate stability zone (deeper than approximately 550–575 mbsl on this margin; Brothers et al., 2014). At approximately 18 km, MX07 crosses the extensive Norfolk seep field (Skarke et al., 2014; Ruppel et al., 2022), which includes dozens of seeps at water depths of approximately 1400 m. The high confidence picks shoal toward the seafloor beneath the Norfolk seep field, consistent with shoaling of the BGHS within gas chimneys (e.g., Yoo et al., 2013). At approximately 180 km along MX09 high confidence picks shoal dramatically beneath the Chincoteague seep field (e.g., Ruppel et al., 2022), where the seafloor is approximately 1100 m deep. Similar shoaling of a feature inter-

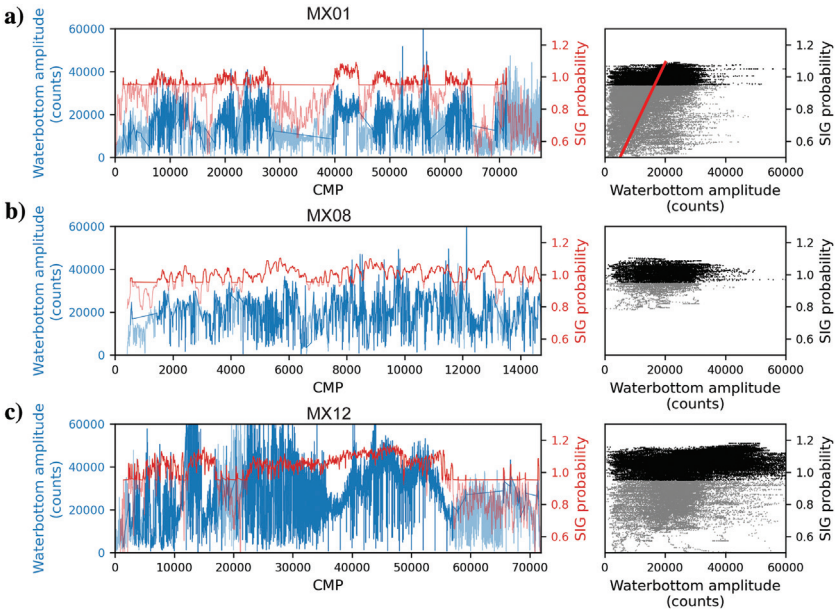

Figure 9. The left part of each panel shows water bottom counts for the seismic amplitude (blue) and confidence (red) for each CMP along a given seismic line. The right part shows the crossplot of confidence and water bottom counts, with the shaded portion being below 0.95 confidence. (a) Results for MX01, the line shown in Figure 8 of the text. The correlation between confidence and signal quality is strong for this line, as shown by the red line on the crossplot. (b) Results for MX08, a line in deeper water but nearly subparallel to MX01. There is no good correlation between signal strength and confidence on this line. (c) MX12 is a dip line in the training data set for the NN and also does not show consistently low confidence for low signal strength.

preted as the top of the gas in the sediments has been noted in the high-resolution MCS data across this seep field (Ruppel et al., 2022). High confidence picks also shoal at approximately 130 and 140 km on MX18, but methane seeps have not yet been detected at these locations despite several modern water column bubble plume surveys across this area (e.g., Baldwin et al., 2020b), including during acquisition of the MATRIX data. Progressing landward, the high confidence zones continue from the deepwater areas beneath the uppermost slope and shoal on all three MAS dip lines. The high confidence zone approaches the seafloor at approximately 0.7 s TWT (approximately 525 mbsl) on MX09 and MX18 and approximately 0.5 s on MX07 (approximately 370 mbsl). Despite numerous USGS surveys for water column gas flare anomalies from 2015 to 2019, seeps that could be the seafloor manifestation of the shoaling high confidence zones on the uppermost slope (approximately 400 mbsl) have so far been detected only along MX09 (Skarke et al., 2014) but not on MX07 or MX18.

MX01 is an approximately 250 km long strike line through the MAS Prospect at a location where the seafloor is approximately 2775 mbsl. For over half of the distance between approximately 40 and 180 km, the NN algorithm identifies a high confidence zone at approximately 0.5 s (approximately 375 m) below the seafloor and close to prominent reflections (Figure 8). Along the rest of MX01, high confidence zones are shallower or absent, often correlating with locations where signal quality degraded. The WBA plotted in Figure 8 show that the intervals with low confidence values or shoaling of the high confidence zone (e.g., across the Accomac Canyon drainage and to the left of the Currituck slide MTD) correspond to lower signal quality on this line. This relationship is verified by crossplotting these factors for MX01 (Figure 9). Figure 9 underscores that this signal quality issue does not affect MX08, a short but high-quality line subparallel to MX01 (Figure 1) and in deeper water (Figure 7). Running the same calculations on the training data set along the Whale Prospect dip line MX12 (Figure 5) also does not reveal a strong correlation between lower confidence and lower signal quality, especially for confidence values exceeding 0.95, the threshold chosen for presenting the NN results. In fact, along some sections of MX12 (CMP > 35,000) signal quality is low but confidence is high.

Hatteras Prospect area

MX02 and MX03 (Figure 10) form a north to south strike line at approximately 3100 mbsl imaging south of the MAS Prospect and then through one of the widest parts of the Hatteras Prospect, respectively. MX02 crosses a series of faults spaced less than a kilometer apart and cutting through much of the section. The MATRIX seismic amplitude data reveal no compelling evidence that these faults tap into the gas at depth or are the locus of gas migration through the sediment. The NN analysis yields intermediate confidence (approximately 0.5) in vertically smeared zones roughly aligned with some of the faults although resolution of the NN image is too low to link the results to individual faults. The only high confidence values on MX02 are on the southern part of the line in the final approximately 10 km section near the tie with MX03. These high confidence values are spatially associated with prominent reflections.

Along MX03, acquisition parameters varied, with the section beyond 70 km having generally higher source levels. The sea state and strong current also affected the quality of the data. The highest confidence zones along MX03 are at 20–40, 70–80, and from 100 km to the end of the line. All of the high confidence picks roughly coincide with strong reflections, particularly at distances greater than 70 km. The high confidence zone in the 20–40 km section deepens more rapidly than the seafloor and cuts across some reflections, implying that these results are likely not highlighting a BSR.

MX04 and MX05 combine to form a crooked dip line in the area between the MAS and Hatteras Prospects. MX04 cuts acutely across Keller Canyon and an MTD at approximately 2300 mbsl, whereas MX05 is a dip line from 1900 mbsl to the top of the slope north of Keller Canyon. MX05 runs parallel to, but does not coincide with, an MTD mapped by Twichell et al. (2009) and terminates at methane seeps on the upper slope. The NN analysis (Figure 10) identifies a continuous high confidence zone at approximately 15 km from the west side of MX04 joining with the east side of MX05. This zone is roughly coincident with strong reflections that mimic seafloor bathymetry. Data are incomplete along the upper slope on MX05, and the available results highlight sparse and laterally discontinuous high confidence zones in this area. This contrasts with the nearly uniform high confidence zones beneath the upper slopes on MX07 and MX09 and the next two dip lines to the north.

Discussion

In this section, we explore the significance of the high confidence zones identified by the NN, implications of the SIGs for local and regional scale petroleum system features, and potential refinements to gas hydrate distribution based on the NN results.

The physical meaning of high confidence picks

Interpreting the physical meaning of high confidence picks that emerge from the NN analyses described in the "Results" section is the fundamental challenge for this study, particularly when these picks are arrayed in a laterally continuous zone that might be interpreted as tracing out an interface. Do these picks indicate BSRs separating HBSs above from underlying gas-charged sediment? Or do high confidence picks coincide with the top of free gas without necessarily implying anything about the existence of gas hydrate? Are there other physical reasons that high confidence picks can highlight a laterally continuous zone in the seismic sections?

One way to calibrate the confidence bands that emerge from the application of the NN to the MATRIX data is by analyzing the qualitative correlation between confidence

results and strong, visually identified BSRs in the Whale Prospect (Figures 5 and 6). For example, in the center of the Whale Prospect, very high confidence (>0.95) NN picks coincide with a prominent BSR identified visually in MATRIX amplitude data (MX12, 13, and 16) and at comparable depths below the seafloor in older seismic data (e.g., Shedd and Hutchinson, 2006). Confidence values are lower (<0.9) where BSRs are harder to discern on the seaward side of the Chesapeake Drift on MX12 and MX13, as explored in the "Discussion" section.

Another way to evaluate the physical significance of the NN-based confidence values is by comparing the results with theoretical bounds on the morphology of the BGHS. For each CMP having the highest smoothed confidence exceeding 0.95, Figure 11 shows the depth (m) below the seafloor of that pick converted using $1.78390878e-04*t^2+7.22966846e-01*t+0.361001632$, where t denotes the TWT in ms relative to the seafloor. This expression was found by fitting velocities determined by traveltime tomography on long-offset USAM

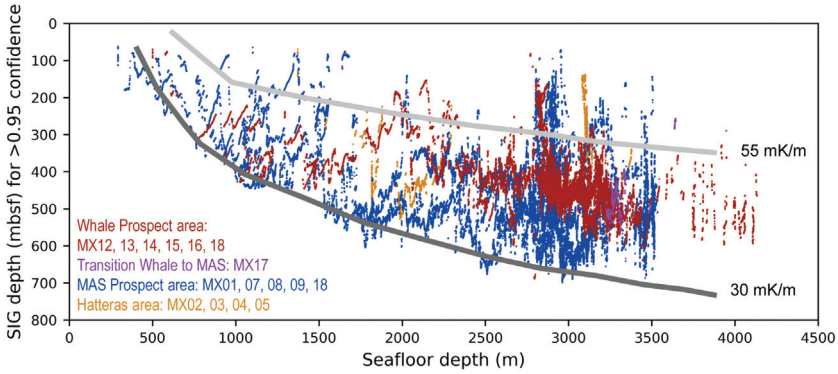

Figure 11. Depth below the seafloor (meters below seafloor or mbsf) of highest confidence for each CMP in the MATRIX lines used for this study, with only points having confidence greater than 0.95 plotted. SIG indicates a seismic indicator of gas. Points are color-coded as shown in the lower left, depending on the general area in which each seismic line was acquired. The heavy light gray and dark gray curves correspond to the theoretical BGHS calculated for two different geotherms (30 and 55 mK/m, respectively) using the parameters defined in the text.

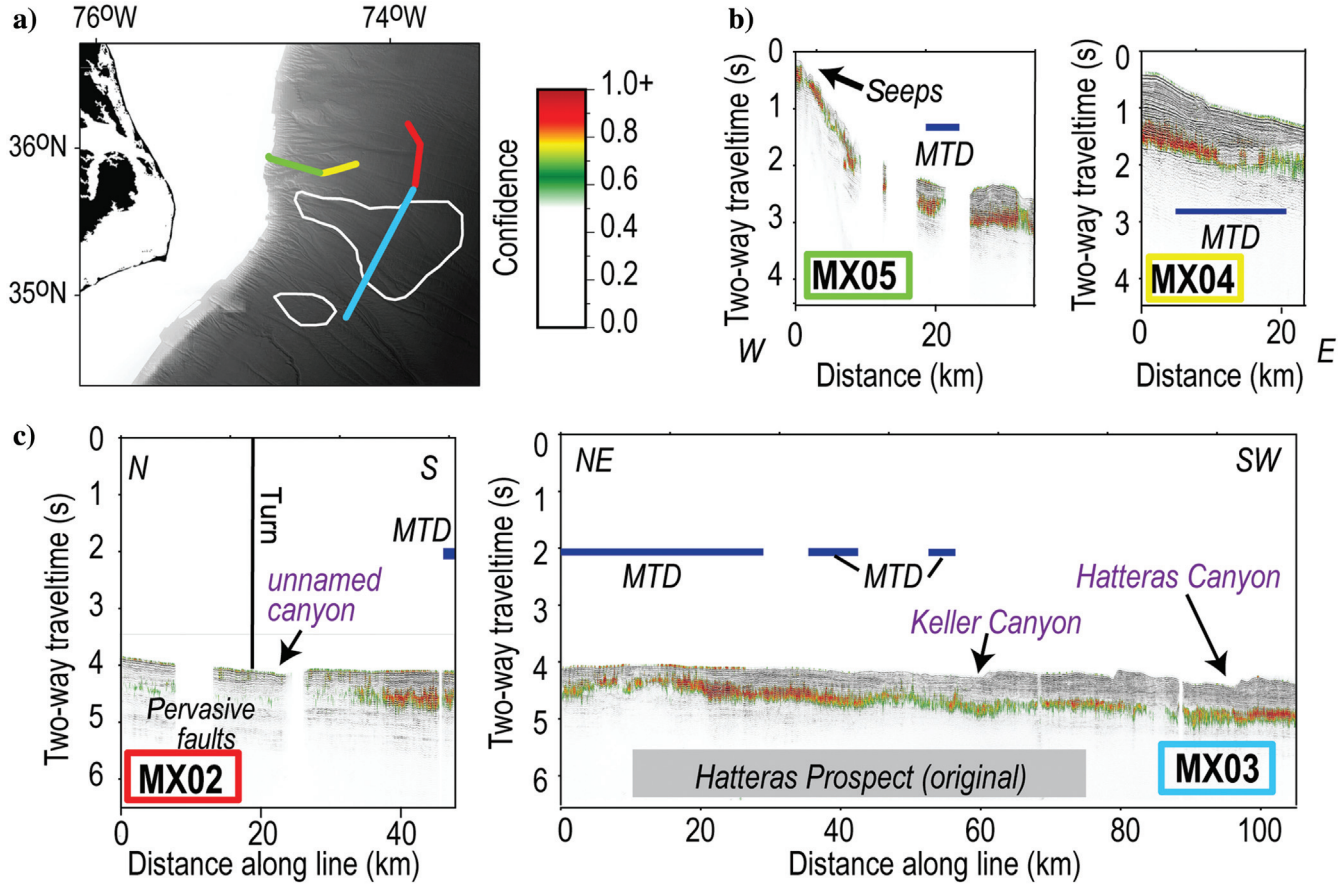

Figure 10. Composite seismic images and neural net results (shown as confidence overlaid on the seismic amplitude data) for the area of the Hatteras Prospect. (a) Map showing the locations of seismic lines in this figure with the outline of the Hatteras Prospect in white and the confidence color scale, which is the same for all parts of the figure. Colors on the map correspond to the seismic lines and the tie lines (vertical lines) on each panel of this figure. (b) Components of a composite dip line made up of MX04 and MX05. The blue lines are the positions of MTDs from Twichell et al. (2009). (c) Components of a composite strike line made of up of MX02 and MX03. The purple labeling refers to deepwater drainages that connect to major upper slope canyons.

seismic data collected by the USGS using large air guns (Arsenault et al., 2017). For comparison, Figure 11 also shows the depth below the seafloor of the BGHS for two geothermal gradients (30°C/km and 55°C/km) using the approach outlined in the "Methods" section. To make the BGHS bounds as conservative (wide) as possible, the bottom water temperature (seafloor boundary condition) at each water depth used for the fit was 1°C colder (for the cold geotherm endmember) or warmer (for the warm geotherm endmember) than that measured at the comparable depth in the water column offshore Virginia for a full ocean-depth conductivity-temperature-depth cast. Across the MATRIX data set, most high confidence picks plot within the BGHS bounds in Figure 11, implying that the features assigned high confidence by the NN analysis could be related to the gas hydrate dynamics.

Based on this calibration of the NN results, we infer that different confidence values correlate with qualitative categories (high, intermediate, and low probability) for the presence of gas hydrate just above the BGHS and/or, more likely, free gas trapped immediately beneath the BGHS. However, it is inappropriate to interpret a confidence interval in the NN results as corresponding to the percentage likelihood that a BSR exists or that gas hydrate is present at that location. For example, a 0.7 confidence value should not be interpreted as indicating that there is a 70% likelihood of a BSR at that depth. We emphasize that the qualitative categories also have an associated uncertainty based on the choice of the threshold value for high probability. If the high confidence threshold were set at 0.9 or 0.925 instead of 0.95, approximately 10% (174 km) or 5.3% (92 km) more of the seismic lines would be included in the high confidence picks, respectively. For a stricter threshold of 0.975 as the high confidence threshold, 6.4% fewer line kilometers (111 km) would be within the high-probability category.

Without borehole logging or drilling to confirm the presence of gas hydrates, high confidence picks produced by the NN for this short-offset MATRIX data set cannot be unequivocally interpreted as indicating the existence of gas hydrate or implying that gas hydrate saturations exceed a certain percentage of pore space. Based on the nature (frequency and amplitude dependence) of the seismic attributes chosen for this analysis, the highest confidence picks are most likely related to the top of the sediments charged with free gas, not necessarily the base of gas hydrate. As discussed by Xu and Ruppel (1999) for homogeneous sediments and as explored in detail by Ruppel and Waite (2020) for a range of scenarios, the actual base of gas hydrate coincides with the top of free gas only when gas is present in excess of local methane solubility in pore space near the thermodynamic stability boundary. All natural sediments are inhomogeneous at some spatial scale, and hydrate often accumulates at higher saturations in layers with higher relative permeability (e.g., diatomaceous layers in hemipelagic ooze and sandier layers interbedded with silts and clays; e.g., Kraemer et al., 2000; Malinverno, 2010; Boswell et al., 2011), even if those layers are shallower than the thermodynamic stability boundary or the top of gas-charged sediments (e.g., Cook and Malinverno, 2013; VanderBeek and Rempel, 2018; Ruppel and Waite, 2020). The interpretation that high confidence picks most likely trace the top of gas-charged sediments is supported by high confidence values that emerge at lower slope unconformities (e.g., on lines MX07 and MX09). These unconformities typically mark lithologic changes, and the associated permeability contrasts could lead to free gas being trapped below.

The NN also identifies high confidence zones below the steepest parts of the upper continental slope (<2000 mbsl) on most dip lines. These upper continental slope high confidence zones are unlikely to have a single explanation. As noted previously, some of the high confidence zones follow stratigraphic layering, bright reflections, and/or unconformities. High confidence at such interfaces is most likely to indicate gas charging. Other high confidence picks cross-cut stratigraphy (e.g., 40–110 km along MX07) and roughly follow the seafloor, implying coincidence with the thermodynamic BGHS. On MX07 and MX09, the shoaling of the high confidence picks beneath the Chincoteague and Norfolk deepwater seep fields is consistent with perturbation of the BGHS across the gas chimneys that feed these seafloor seeps and that have been identified in high-resolution imagery (e.g., Ruppel et al., 2022).

Implications for regional gas hydrate and/or shallow free gas distribution

Although the MATRIX data do not cover as much area as the USGS legacy data used by BOEM (Frye et al., 2013) to map the BSR polygons shown in Figures 1 and 13, the NN results obtained from the analysis of the new data set still provide critical information to refine the distribution of seismic features that may be related to the presence of shallow free gas or gas hydrate. For the polygons corresponding to the Whale, MAS, and Hatteras Prospects, the maximum smoothed confidence values exceed 0.95 at the SIGs for 86.3%, 70.9%, and 26.4%, respectively, of the CMPs along the segments of the intersecting MATRIX lines. Overall, only 52.4% of the CMP confidence values exceed even 0.85 within the Hatteras Prospect. These SIG results confirm inferences about BSRs made earlier based on the visual analysis of MATRIX (e.g., Majumdar et al., 2019; Ruppel et al., 2019) and legacy (Frye et al., 2013) seismic data: BSRs are well developed within the Whale Prospect, but similar features are harder to discern in the MAS Prospect and especially near the Hatteras Prospect. These results also provide greater confidence that some of the stratigraphy-parallel reflections identified through visual analysis in the MAS and Hatteras Prospects have the characteristics of seismic features associated with the top of free gas.

Within a marine petroleum systems framework (e.g., Hutchinson et al., 2008; Ruppel et al., 2019), the pattern of SIG (and BSRs) along the northern USAM could

reflect variations in the characteristics of either the gas charge or the so-called container, which here refers to the sediments that host and sometimes trap free gas and gas hydrate. For gas charge, seismic methods cannot distinguish microbial from thermogenic methane. Thus, any assessment of possible spatial variations in gas charge that could produce differences in SIG/BSR characteristics must focus on physical differences. To first order, stronger BSRs or SIGs with higher confidence may be associated with larger volumes of free gas or gas hydrate. Spatial variations in gas charge could be related to the thickness of the sedimentary section over the basement, assuming that the thicker sediments may contain more organic carbon to drive the production of microbial methane. Analysis of the correlation between USAM sediment thickness and maximum confidence values obtained at each MATRIX CMP shows that median SIG confidence values exceed 0.9 at CMPs where the sediment thickness is approximately 4200 m or greater (Figure 12a). However, along individual seismic lines, the 4200 m condition is necessary for confidence to exceed 0.9 but not sufficient. For example, on the Hatteras area line MX02, sediment thickness is approximately 5750–6750 m, but median confidence never reaches 0.9. On dip line MX18, a high-quality line through the northern end of the MAS Prospect, sediment thicknesses fall in bins from approximately 5250 to 11,250 m, and median confidence exceeds 0.9 for sediment thicknesses less than 9250 m. These observations imply that gas charge, here interpreted through the proxy of sediment thickness, may not be the only factor linked to high confidence in the ML results.

In the petroleum systems framework, variations in the characteristics of the free gas/gas hydrate container also may explain some of the spatial differences in the SIG confidence values shown in Figures 1 and 11. The quality of the container is related to the lithology and sedimentary processes, as well as structural features that may contribute to the focusing or trapping of migrating fluids. For example, coarse sands are known to host the highest saturations of gas hydrate in other marine margin settings (Torres et al., 2008; Boswell et al., 2012). However, the well-studied Blake Ridge sediment drift deposit has prominent BSRs but low gas hydrate saturations within fine-grained sediments (e.g., Holbrook et al., 1996; Collett and Ladd, 2000).

To assess these lithologic relationships for the MATRIX data set, we examine SIG confidence values as a function of sand content inferred by BOEM (Frye et al., 2013) for the upper 2000 ft (approximately 610 m) of the sedimentary section. Within the BOEM-defined prospects, Figure 12b demonstrates that the Whale Prospect, followed by the MAS Prospect, has higher average sand content in the upper approximately 610 m than the Hatteras Prospect does. For the whole MATRIX data set, which includes the BOEM prospects and adjacent areas imaged by the survey, sand content greater than approximately 27.5% is associated with median SIG confidence values greater than 0.9 (Figure 12c). The relationship does not hold along the individual lines or in the areas of individual prospects though. For the Whale Prospect area, median SIG confidence values exceed 0.9 for sand content of 12.5–27.5% and greater than 37.5% but not for intermediate sand contents. Near the MAS

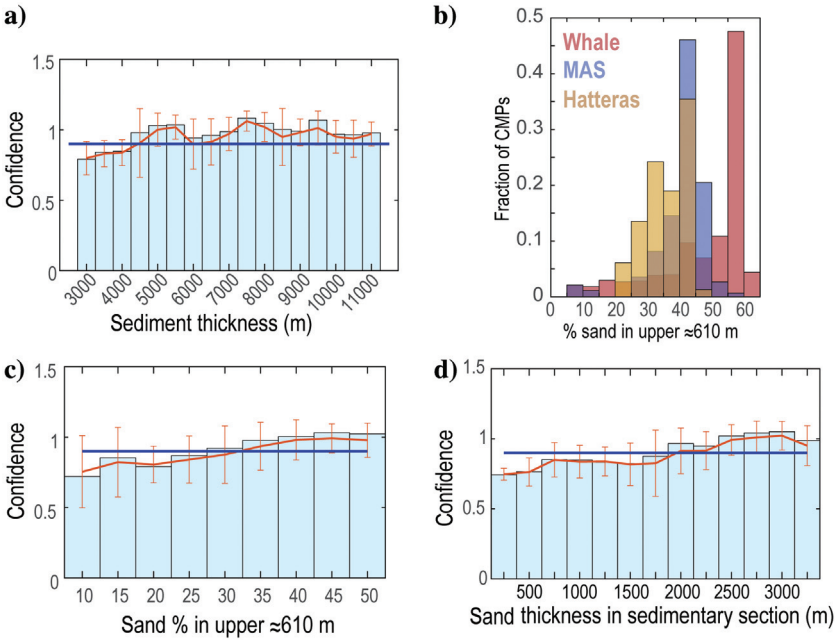

Figure 12. Assessment of the results of the neural net analysis of the MATRIX seismic data in terms of the total petroleum system focuses on the possible gas charge (to first order related to sediment thickness) and the reservoir quality (related to sand content). (a) Bars show median value of confidence determined by the NN for all MATRIX CMPs as a function of binned sediment thickness as determined from USGS legacy seismic data. The red line is the average, and standard deviation of the confidence values in each bin is shown. The blue line represents a confidence value of 0.9. (b) Histogram showing the fraction of MATRIX CMPs intersecting the Whale, MAS, and Hatteras Prospects and having a given percentage sand in the uppermost approximately 610 m based on the BOEM mapping (Frye et al., 2013). The Hatteras Prospect is far more poorly sampled by MATRIX lines than the MAS and Whale Prospects. However, the overall result shows that the Whale Prospect has the highest sand content, which is skewed toward higher values but with a broad range. The MAS Prospect is dominated by intermediate sand contents and also has a spread of values, whereas the MATRIX lines cross the Hatteras Prospect where sand content is on average lower but constrained to a smaller range of values. (c) The same as (a), with the maximum confidence at each CMP binned according to the sand percentage in uppermost approximately 610 m of sediment (Frye et al., 2013). (d) The same in (a), with the maximum confidence at each CMP binned by multiplying the percentage sand at each location (Frye et al., 2013) by the total thickness of sediment at a location to determine the composite sand thickness at each CMP.

Prospect, the 0.9 median confidence threshold is reached at sand content greater than 27.5%, and in the Hatteras area, the 0.9 median confidence is not met for any sand content values, which span the range from 17.5% to 37.5%.

Although clear patterns do not emerge from this analysis, the area near the Whale Prospect has the highest overall SIG confidence values, the strongest visually identifiable BSRs, and the highest sand content, in addition to the structural trap created by the mounding of seafloor sediments deposited in a relatively quiescent setting of the Chesapeake Drift. The Hatteras area, with its relatively low sand content, pervasive mass wasting deposits, and strong currents (Gulf Stream and Deep Western Boundary Current) has low overall SIG confidence values and poor conditions for the development of gas hydrates or accumulations of free gas.

We also conducted analyses that combine information about sediment thickness (Figure 12d) or thicknesses of parts of the sedimentary section (e.g., depth to the top of the Pliocene and thickness of Pliocene to top of the Cretaceous interval; Frye et al., 2013) with the sand content in the upper 2000 ft (approximately 610 m; Frye et al., 2013) to test whether a combination of gas charge proxies and container information could explain patterns in the SIG confidence values. For these calculations, we multiplied the percentage of sand in the upper approximately 610 m from Frye et al. (2013) by sediment thickness to approximate how much of the whole interval is represented by sand. For example, if a CMP location has 4000 m of sediment and 25% sand in the upper approximately 610 m, we used 1000 m as the thickness of the sand at that location, assuming sediments deeper than approximately 610 m had the same lithologic distribution as the shallower section. Using this approach, we found that the median SIG confidence values showed no dependence on the assumed thickness of the sand section within the younger than Pliocene sediments or the Pliocene to Cretaceous section. However, for the entire sedimentary section at each CMP, median SIG confidence only exceeds 0.9 when more than approximately 1900 m of sand was present, as shown in Figure 12d. This crude measure implies that a combination of gas charge (sediment thickness) and container quality (lithology) might be used as a predictor for high-probability SIGs within the MAB.

Implications of local variations in SIG confidence values

The regional patterns of SIGs discussed previously may reflect broad changes in factors such as sediment thickness and sediment type, but local variations in SIG confidence values are more likely to result from features such as shingled faults in the shallow section or lithologic changes associated with MTDs near the seafloor or deepwater canyons.

Figures 6–8 and 10 label deepwater drainages that are the extensions of shelf-break canyons on the lower continental slope and the continental rise. We previously noted that the Baltimore Canyon deepwater drainage truncates high confidence zones in the Whale Prospect area and also is associated with the absence of a high confidence zone at the beginning of MX01. However, the many deepwater canyon drainages crossed by the remainder of MX01 (Figure 8) are not consistently associated with the disruption of high confidence zones. Across the deepwater Phoenix Canyon, the highest confidence picks are continuous and retain high-probability values. The high confidence zone remains continuous but is deflected downward beneath the deepwater Washington and Norfolk drainages (Figure 8).

The presence of MTD, which typically add sediment to the seafloor and temporarily lower thermal gradients as they develop (e.g., Ruppel and Waite, 2020), also shows no consistent relationship with the lateral continuity or absolute confidence values in the data set. For example, MTDs crossed by MX01 at distances up to 180 km along the line are associated with uniformly high confidence in a zone continuous with adjacent parts of the line in two of the three cases. At the third MTD encountered along MX01 (approximately 65 km distance), the high confidence zone disappears within

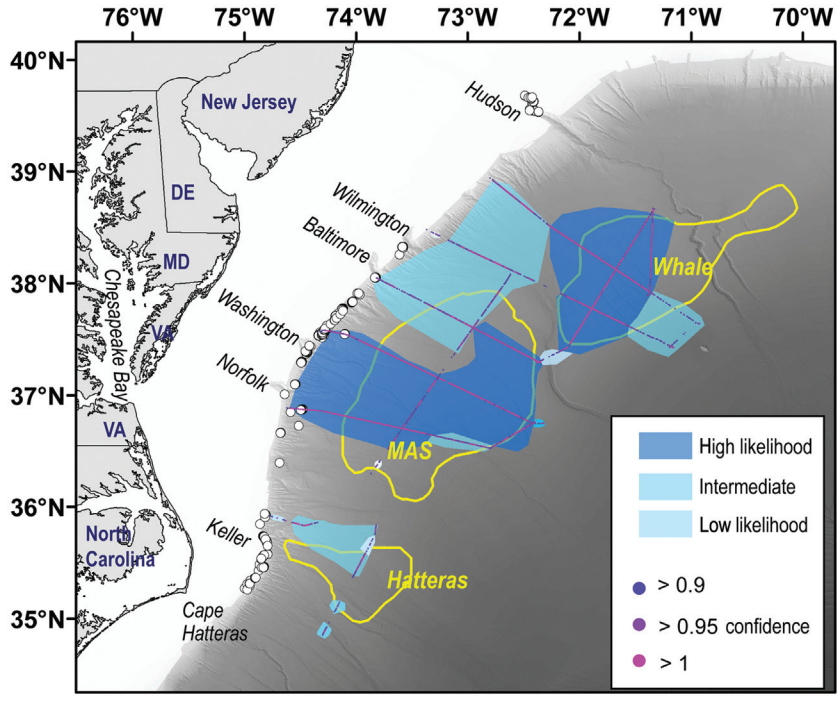

Figure 13. Regionalization of the results from applying the neural net framework to the MATRIX seismic data along the lines shown. The yellow polygons outline the gas hydrate prospects identified by BOEM (Frye et al., 2013) based on mapping of BSRs in legacy seismic amplitude data. Only confidence levels greater than 0.9 are shown. The compiled results expand the area with SIG on this margin relative to the original BSR polygons.

the MTD, not at its edges. Only where MX01 crosses the Currituck slide, a large volume MTD (Hill et al., 2017) known to be associated with BSRs along parts of its length (e.g., Ruppel et al., 2022), is the edge of the MTD correlated with the loss of high confidence.

Refining gas hydrate prospects

The high confidence zones shown in Figure 13 expand the potential area for shallow gas features and possibly gas hydrates on the northern USAM beyond the polygons first mapped by BOEM and also show that the BOEM polygons may need to be redrawn to shrink gas hydrate prospects where the NN algorithm did not detect high confidence for SIGs in the MATRIX data. The MATRIX data set does not have as complete areal coverage as the legacy USGS seismic data used by BOEM in construction of the original BSR map, meaning that only qualitative comparisons are possible between the two sets of results.

The map (Figure 13) derived by applying an NN approach to the MATRIX data to identify SIGs expands the overall area possibly associated with hosting gas or hydrate-related features. For this analysis, we assess the likelihood of SIGs being present based on the lateral continuity and uniformity of NN-derived confidence values greater than 0.9 at each CMP. High likelihood areas have nearly continuous confidence values of 0.95 or greater along the seismic lines. Intermediate likelihood zones have confidence that typically exceed 0.9 nearly continuously along the seismic lines but with more 0.9–0.95 values than in the high likelihood zones. Lower likelihood areas still have SIGs in places, but the high confidence zones are laterally discontinuous, which may indicate that SIGs are only patchy.

The most important difference between the new map and the originally defined BSR-based prospects that BOEM generated (BOEM, 2012; Frye et al., 2013) is the expansion of the MAS Prospect to include a high likelihood area between the upper continental slope and approximately 2000 mbsl. This expanded MAS Prospect encompasses the high confidence values found along MX07 and MX09 and may extend from north of Washington Canyon to south of Norfolk Canyon along the USAM. The new map also reveals a landward expansion of the main part of the Whale Prospect in a high likelihood zone along MX12. Most of the upper slope landward of the Whale Prospect (MX12 and MX13) and landward of the northern part of the MAS Prospect (MX18) is categorized as an intermediate likelihood zone, with SIGs not as pronounced or laterally continuous as along MX07 and MX09. This area has not formerly been included in BSR maps except for the part of line 18 that lay within the original MAS Prospect as mapped by Frye et al. (2013).

Due to sea state, weather, and currents, we were not able to collect MATRIX imagery through much of the Hatteras Prospect. The data that we analyzed confirm that part of the Hatteras Prospect has intermediate likelihood for SIGs, consistent with BOEM's determination that this prospect had less certain BSRs than the Whale Prospect or Blake Ridge. Our map potentially expands the area of intermediate likelihood to include the upper slope just north of the Hatteras Prospect as well.

The refinement of MAB gas hydrate prospects shown in Figure 13 necessarily omits areas not traversed by MATRIX data. For example, Ruppel et al. (2022) note that a dip line acquired along the Currituck slide, which lies between the Hatteras and MAS Prospects, has evidence for BSRs and consider BSR features on a legacy seismic line on the southern New England margin (Sonema of Figure 1, inset) east of the Whale Prospect as well.

Conclusion

We applied a supervised NN framework to newly acquired high-resolution MCS data to identify seismic objects associated with the presence of free gas and/or gas hydrates in marine sediments on the northern USAM between Cape Hatteras and Hudson Canyon. BSRs can be difficult to discern through visual analysis of seismic amplitude data in parts of the study area, and the NN approach, which used seismic attributes based primarily on frequency and amplitude characteristics, allowed us to identify SIG, which we interpret as features marking the top of free gas or possibly related to the presence of gas hydrate. The seismic attributes found to be the most diagnostic of SIG features were sweetness, envelope weighted instantaneous frequency, envelope slope, and low-pass amplitude. The SIGs were correlated with clear BSRs in the Whale Prospect, corresponded to strong reflections in some other parts of the study area, and shoaled beneath known deepwater seep sites, all characteristics that would indicate that the SIGs might be interpreted as BSRs in some locations. In addition, the depths of the highest confidence SIGs at each CMP in the data set lie mostly within broad bounds on theoretical BGHS for this margin. High-confidence SIGS are more likely to be associated with higher sand content (which has only been determined in the uppermost approximately 610 m of the section), but the interpretation does not hold for individual lines and may be biased by the relatively high sand content and predominance of high-confidence SIGs in the Whale Prospect. Within a petroleum systems framework, the higher confidence SIGs appear to correlate with a combination of sediment thickness and sand content. This implies that the container size and characteristics and the gas charge may play a role in our detection of gas-related features.

Our analysis determined high confidence for the presence of shallow gas or possibly gas hydrate in Whale Prospect and parts of the MAS Prospect. The neural net also revealed SIG features beneath the upper continental slope landward of the approximately 2000 m isobath and extending nearly to the shelf break, implying that the area associated with shallow gas and/or hydrate on the northern USAM is likely significantly larger than previously mapped. In some places, the SIGs as determined by the NN were laterally discontinuous, which could reflect variations in gas charge and changes in the character of the sediments (e.g., across deepwater canyons). Other

gaps in high-confidence SIGs or unexplained shoaling of SIGs appear to be related to changes in acquisition parameters, especially along the first line collected (MX01) for this data set.

Supervised deep-learning approaches using NN hold promise for the identification of SIGs in seismic data sets where features such as BSRs are difficult to map based solely on visual analysis of amplitude data. Supervised NN does have some disadvantages, including the necessity of training on a data subset in which the desirable features (e.g., BSRs) are well developed and the difficulty of applying an NN trained on a specific seismic data set to another data set acquired with different parameters (e.g., numbers of guns and array geometry). Nonetheless, the NN approach used here provides confidence that features associated with shallow gas and/or gas hydrate are significantly more widespread on the northern USAM than could be determined based on the traditional analysis of seismic amplitude imagery alone and that this technique could be extended to map SIGs in legacy seismic data in this area or in other areas where gas hydrate is known to be present, but BSRs are not widely mapped.

Acknowledgments

The MATRIX seismic program was sponsored by DOE-USGS Interagency Agreement DE-FE0023495 and BOEM-USGS Interagency Agreement M17PG00041 to the USGS Gas Hydrates Project and by the USGS Coastal and Marine Hazards and Resources Program (CMHRP). DOE-USGS Interagency Agreement 89243320SFE000013 supported analyses that led to the completion of this study. We thank the crew of the *R/V Hugh R. Sharp*; J. Swallow and T. Deering of the University of Delaware Marine Operations office; and W. Baldwin, D. Foster, E. Moore, C. Worley, W. Danforth, T. O'Brien, T. Elfers, P. Dal Ferro, D. Powers, J. McKee, and P. J. Bernard of the USGS for assistance with cruise preparations and/or shipboard operations. Scripps Institute of Oceanography (E. Ellett and K. Pedrie), Lamont Doherty Earth Observatory (J. Rupert), and Stark Industries provided equipment, advice, and other assistance to MATRIX. Seismic data were processed by W. Baldwin and D. Foster under the direction of N.C.M. We thank BOEM colleagues (W. Shedd, M. Frye, and S. Palmes) and D. Hutchinson (USGS) for discussions and access to data sets, J. Kluesner for advice on machine learning and comments that improved the manuscript, J. Chaytor for legacy shapefiles, and I. Pecher for helpful review comments. H. Smith (National Science Foundation) was instrumental in advising on marine seismic permitting that made MATRIX possible. U.M. worked at the USGS with support from a postdoctoral fellowship provided by the Woods Hole Oceanographic Institution. Any use of trade, firm, or product names is for descriptive purposes only and does not imply endorsement by the U.S. Government.

Data and materials availability

Data associated with this research are available and can be accessed via the following URLs: https://doi.org/10.5066/P91WP1RZ, https://doi.org/10.5066/P97LBUSP, and https://doi.org/10.5066/P9Y1MSTN.

References

Aminzadeh, F., D. Connolly, R. Heggland, P. Meldahl, and P. de Groot, 2002, Geohazard detection and other applications of chimney cubes: The Leading Edge, **21**, 681–685, doi: 10.1190/1.1497324.

Arsenault, M. A., N. C. Miller, D. R. Hutchinson, W. E. Baldwin, E. M. Moore, D. S. Foster, T. F. O'Brien, and W. F. Fortin, 2017, Geophysical data collected along the Atlantic Continental Slope and Rise 2014, U.S. Geological Survey Field Activity 2014-011-FA, Cruise MGL1407: U.S. Geological Survey data release, doi: 10.5066/F7V69HHS.

Baldwin, W. E., D. S. Foster, E. M. Bergeron, P. Dal Ferro, J. A. McKee, E. M. Moore, A. R. Nichols, T. F. O'Brien, D. Powers, N. C. Miller, and C. D. Ruppel, 2020a, Multichannel seismic-reflection and navigation data collected using Sercel GI guns and Geometrics GeoEel digital streamers during the Mid-Atlantic Resource Imaging Experiment (MATRIX), USGS Field Activity 2018-002-FA: U.S. Geological Survey data release, doi: 10.5066/P91WP1RZ.

Baldwin, W. E., D. S. Foster, E. M. Bergeron, P. Dal Ferro, J. A. McKee, E. M. Moore, A. R. Nichols, T. F. O'Brien, D. Powers, N. C. Miller, and C. D. Ruppel, 2021, Sonobuoy seismic and navigation data collected using Sercel GI guns and Ultra Electronics expendable sonobuoys during the Mid-Atlantic Resource Imaging Experiment (MATRIX), USGS Field Activity 2018-002-FA: U.S. Geological Survey data release, doi: 10.5066/P97LBUSP.

Baldwin, W. E., E. M. Moore, C. R. Worley, A. R. Nichols, and C. D. Ruppel, 2020b, Marine geophysical data collected to support methane seep research along the U.S. Atlantic continental shelf break and upper continental slope between the Baltimore and Keller Canyons during U.S. Geological Survey Field Activities 2017-001-FA and 2017-002-FA: U.S. Geological Survey data release, doi: 10.5066/P9Y1MSTN.

Bedle, H., 2019, Seismic attribute enhancement of weak and discontinuous gas hydrate BSRs in the Pegasus Basin, New Zealand: Interpretation, **7**, no. 3, SG11–SG22, doi: 10.1190/INT-2018-0222.1.

Berrar, D., 2019, Cross-validation, in Ranganathan, S., M. Gribskov, K. Nakai, and C. Schonbach, eds., Encyclopedia of bioinformatics and computational biology: Elsevier 1, 542–545, doi: 10.1016/B978-0-12-809633-8.20349-X.

BOEM, 2012, Assessment of in-place gas hydrate resources of the lower 48 United States outer continental shelf, Fact Sheet, RED2012-01, 4, https://www.boem.gov/sites/default/files/uploadedFiles/BOEM/Oil_and_Gas_Energy_Program/Resource_Evaluation/Gas_Hydrates/BOEM-FactSheetRED_2012-01.pdf, accessed 10 Mar 2018.

Boswell, R., M. Frye, D. Shelander, W. Shedd, D. McConnell, and A. Cook, 2012, Architecture of gas-hydrate-bearing sands from Walker Ridge 313, Green Canyon

955, and Alaminos Canyon 21: Northern deepwater Gulf of Mexico: Marine and Petroleum Geology, **34**, 134–149, doi: 10.1016/j.marpetgeo.2011.08.010.

Boswell, R., K. Rose, T. S. Collett, M. Lee, W. Winters, K. A. Lewis, and W. Agena, 2011, Geologic controls on gas hydrate occurrence in the Mount Elbert prospect, Alaska North Slope: Marine and Petroleum Geology, **28**, 589–607, doi: 10.1016/j.marpetgeo.2009.12.004.

Brothers, D., C. Ruppel, J. Kluesner, U. ten Brink, J. Chaytor, J. Hill, B. Andrews, and C. Flores, 2014, Seabed fluid expulsion along the upper slope and outer shelf of the U.S. Atlantic continental margin: Geophysical Research Letters, **41**, 96–101, doi: 10.1002/2013GL058048.

Chenin, J., and H. Bedle, 2020, Multi-attribute machine learning analysis for weak BSR detection in the Pegasus Basin, offshore New Zealand: Journal of Geophysical Research: Oceans, **41**, 1–20, doi: 10.1007/s11001-020-09421-x.

Chopra, S., and K. Marfurt, 2005, Seismic attributes — A historical perspective: Geophysics, **70**, no. 5, 3SO–28SO, doi: 10.1190/1.2098670.

Chopra, S., and K. Marfurt, 2008, Emerging and future trends in seismic attributes: The Leading Edge, **27**, 298–318, doi: 10.1190/1.2896620.

Collett, T. S., and J. Ladd, 2000, Detection of gas hydrate with downhole logs and assessment of gas hydrate concentrations (saturations) and gas volumes on the Blake Ridge with electrical resistivity log data: Proceedings of the Ocean Drilling Program, Scientific Results 164, 179–191, doi: 10.2973/odp.proc.sr.164.219.2000.

Cook, A. E., and A. Malinverno, 2013, Short migration of methane into a gas hydrate-bearing sand layer at Walker Ridge, Gulf of Mexico: Geochemistry, Geophysics, Geosystems, **14**, 283–291, doi: 10.1002/ggge.20040.

dGB Earth Sciences, 2021, OpendTect software, with neural networks plugin, https://www.dgbes.com/index.php/software/opendtect, accessed 4 Aug 2021.

Dixon, J. F., R. J. Steel, and C. Olariu, 2012, River-dominated, shelf-edge deltas: Delivery of sand across the shelf break in the absence of slope incision: Sedimentology, **59**, 1133–1157, doi: 10.1111/j.1365-3091.2011.01298.x.

Ebuna, D. R., J. W. Kluesner, K. J. Cunningham, and J. H. Edwards, 2018, Statistical approach to neural network imaging of karst systems in 3D seismic reflection data: Interpretation, **6**, no. 3, B15–B35, doi: 10.1190/INT-2017-0197.1.

Frye, M., W. Shedd, and J. Schuenemeyer, 2013, Gas hydrate resource assessment Atlantic Outer Continental Shelf: Spatial analysis of inputs and outputs; graphical and mathematical description of models and sub-models: Bureau of Ocean Energy Management, http://www.boem.gov/BOEM-Report-RED/, accessed 8 Apr 2021.

Hart, B. S., 2008, Channel detection in 3-D seismic data using sweetness: AAPG Bulletin, **92**, 733–742, doi: 10.1306/02050807127.

Heggland, R., P. Meldahl, B. Bril, and P. de Groot, 1999, The chimney cube, an example of semi-automated detection of seismic objects by directive attributes and neural networks: Part II; Interpretation: 69th Annual International Meeting, SEG, Expanded Abstracts, 935–940, doi: 10.1190/1.1821263.

Heggland, R., 2004, Definition of geohazards in exploration 3-D seismic data using attributes and neural-network analysis: AAPG Bulletin, **88**, 857–868, doi: 10.1306/02040404019.

Hien, D. H., S. Jang, and Y. Kim, 2010, Multiple seismic attribute analyses for determination of bottom simulating reflector of gas hydrate seismic data in the Ulleung Basin of Korea: Marine Geophysical Researches, **31**, 121–132, doi: 10.1007/s11001-010-9081-1.

Hill, J. C., D. S. Brothers, B. K. Craig, U. S. ten Brink, J. D. Chaytor, and C. H. Flores, 2017, Geologic controls on submarine slope failure along the central U.S. Atlantic margin: Insights from the Currituck Slide Complex: Marine Geology, **385**, 114–130, doi: 10.1016/j.margeo.2016.10.007.

Hill, J. C., D. S. Brothers, M. J. Hornbach, D. E. Sawyer, D. J. Shillington, and A. Bécel, 2019, Subsurface controls on the development of the Cape Fear Slide Complex, central US Atlantic Margin: Geological Society of London, Special Publications 477, doi: 10.1144/SP477.17.

Hill, J. C., N. W. Driscoll, J. K. Weissel, and J. A. Goff, 2004, Large-scale elongated gas blowouts along the U.S. Atlantic margin: Journal of Geophysical Research: Solid Earth, **109**, B09101, doi: 10.1029/2004JB002969.

Holbrook, W. S., H. Hoskins, W. T. Wood, R. A. Stephen, and D. Lizarralde, 1996, Methane hydrate and free gas on the Blake Ridge from vertical seismic profiling: Science, **273**, 1840–1843, doi: 10.1126/science.273.5283.1840.

Hornbach, M. J., D. M. Saffer, W. S. Holbrook, H. J. A. Van Avendonk, and A. R. Gorman, 2008, Three-dimensional seismic imaging of the Blake Ridge methane hydrate province: Evidence for large, concentrated zones of gas hydrate and morphologically driven advection: Journal of Geophysical Research, **113**, B07101, doi: 10.1029/2007JB005392.

Hush, D. R., and B. G. Horne, 1993, Progress in supervised neural networks: IEEE Signal Processing Magazine, **10**, 8–39, doi: 10.1109/79.180705.

Hutchinson, D. R., D. Shelander, J. Dai, D. McConnell, W. Shedd, M. Frye, C. Ruppel, R. Boswell, E. Jones, T. S. Collett, K. Rose, B. Dugan, W. Wood, and T. Latham, 2008, Site selection for DOE/JIP gas hydrate drilling in the northern Gulf of Mexico: Proceedings of the 6th International Conference on Gas Hydrates 12, doi: 10.14288/1.0041022.

Jeong, T., J. Byun, H. Choi, and D. Yoo, 2014, Estimation of gas hydrate saturation in the Ulleung basin using seismic attributes and a neural network: Journal of Applied Geophysics, **106**, 37–49, doi: 10.1016/j.jappgeo.2014.04.006.

Kim, K. J., B. Yi, N. Kang, D.-G. Yoo, K. Shin, and Y. Cho, 2014, Seismic attribute analysis of the indicator for gas

hydrate occurrence in the Northwest Ulleung Basin, East Sea: Geophysics and Geophysical Exploration, **17**, 216–230, doi: 10.7582/GGE.2014.17.4.216.

Kluesner, J. W., and D. S. Brothers, 2016, Seismic attribute detection of faults and fluid pathways within an active strike-slip shear zone: New insights from high-resolution 3D P-Cable™ seismic data along the Hosgri Fault, offshore California: Interpretation, **4**, no. 1, SB131–SB148, doi: 10.1190/INT-2015-0143.1.

Kraemer, L. M., R. M. Owen, and G. R. Dickens, 2000, Lithology of the upper gas hydrate zone, Blake Outer Ridge: A link between diatoms, porosity, and gas hydrate: Proceedings of the Ocean Drilling Program, Scientific Results 164, 229–236, doi: 10.2973/odp.proc.sr.164.221.2000.

Ligtenberg, J. H., 2005, Detection of fluid migration pathways in seismic data: Implications for fault seal analysis: Basin Research, **17**, 141–153, doi: 10.1111/j.1365-2117.2005.00258.x.

Majumdar, U., A. E. Cook, W. Shedd, and M. Frye, 2016, The connection between natural gas hydrate and bottom-simulating reflectors: Geophysical Research Letters, **43**, 7044–7051, doi: 10.1002/2016GL069443.

Majumdar, U., N. C. Miller, C. D. Ruppel, W. E. Baldwin, D. S. Foster, M. Frye, S. Palmes, and W. W. Shedd, 2019, Refining gas hydrate distribution on the U.S. Mid-Atlantic margin using modern seismic data: AGU Fall Meeting Abstracts, OS43A-03.

Malinverno, A., 2010, Marine gas hydrates in thin sands that soak up microbial methane: Earth and Planetary Science Letters, **292**, 399–408, doi: 10.1016/j.epsl.2010.02.008.

Manspeizer, W., 1988, Triassic-Jurassic rifting and opening of the Atlantic: An overview: Developments in Geotectonics, **22**, 41–79, doi: 10.1016/B978-0-444-42903-2.50008-7.

Markl, R. G., G. M. Bryan, and J. I. Ewing, 1970, Structure of the Blake-Bahama outer ridge: Journal of Geophysical Research, **75**, 4539–4555, doi: 10.1029/JC075i024p04539.

Marzoli, A., P. R. Renne, E. M. Piccirillo, M. Ernesto, G. Bellieni, and A. De Min, 1999, Extensive 200-million-year-old continental flood basalts of the Central Atlantic Magmatic Province: Science, **284**, 616–618, doi: 10.1126/science.284.5414.616.

Meldahl, P., R. Heggland, B. Bril, and P. de Groot, 1999, The chimney cube, an example of semi-automated detection of seismic objects by directive attributes and neural networks: Part I; Methodology: 69th Annual International Meeting, SEG, Expanded Abstracts, 931–934, doi: 10.1190/1.1821262.

Meldahl, P., R. Heggland, B. Bril, and P. de Groot, 2001, Identifying faults and gas chimneys using multiattributes and neural networks: The Leading Edge, **20**, 474–482, doi: 10.1190/1.1438976.

Paull, C. K., R. Matsumoto, and P. J. Wallace, et al., 1996, Proceedings of the Ocean Drilling Program: Initial Reports, 164, Ocean Drilling Program, doi: 10.2973/odp.proc.ir.164.1996.

Radovich, B. J., and R. B. Oliveros, 1998, 3-D sequence interpretation of seismic instantaneous attributes from the Gorgon Field: The Leading Edge, **17**, 1286–1293, doi: 10.1190/1.1438125.

Ruppel, C., N. C. Miller, M. Frye, W. E. Baldwin, D. S. Foster, W. Shedd, and S. Palmes, 2019, U.S. Mid-Atlantic resource imaging experiment (MATRIX) constrains gas hydrate distribution, DOE-NETL Fire in the Ice: Newsletter, 19, 6–8, https://www.netl.doe.gov/sites/default/files/publication/MHNews_2019_Spring.pdf, accessed 1 Aug 2020.

Ruppel, C. D., W. Shedd, N. C. Miller, J. Kluesner, M. Frye, and D. R. Hutchinson, 2022, Chapter 24: U.S. Atlantic Margin gas hydrates, *in* J. Mienert, C. Berndt, A. Tréhu, A. Camerlenghi, and C.-S. Liu, eds., World atlas of submarine gas hydrates in continental margins: Springer, 287–302, doi: 10.1007/978-3-030-81186-0.

Ruppel, C. D., and W. F. Waite, 2020, Timescales and processes of methane hydrate formation and breakdown, with application to geologic systems: Journal of Geophysical Research: Solid Earth, **125**, e2018JB016459, doi: 10.1029/2018JB016459.

Russell, B. H., 2004, The application of multivariate statistics and neural networks to the prediction of reservoir parameters using seismic attributes: Ph.D. thesis, University of Calgary.

Satyavani, N., K. Sain, M. Lall, and B. Kumar, 2008, Seismic attribute study for gas hydrates in the Andaman offshore India: Marine Geophysical Researches, **29**, 167–175, doi: 10.1007/s11001-008-9053-x.

Shedd, W. W., and D. R. Hutchinson, 2006, Gas hydrate potential of the Mid Atlantic outer continental shelf, DOE-NETL Fire in the Ice: Newsletter, 6, 8–9, https://www.netl.doe.gov/sites/default/files/publication/HMNewsFall06.pdf, accessed 13 Aug 2020.

Skarke, A., C. Ruppel, M. Kodis, D. Brothers, and E. Lobecker, 2014, Widespread methane leakage from the sea floor on the northern US Atlantic margin: Nature Geoscience, **7**, 657–661, doi: 10.1038/ngeo2232.

Sloan, E. D., and C. Koh, 2007, Clathrate hydrates of natural gases, 3rd ed.: CRC Press.

Thomas, W., 2006, Tectonic inheritance at a continental margin: GSA Today, **16**, 4–11, doi: 10.1130/1052-5173(2006)016[4:TIAACM]2.0.CO;2.

Tonn, R., 2002, Neural network seismic reservoir characterization in a heavy oil reservoir: Geophysics, **21**, 309–312, doi: 10.1190/1.1463783.

Torres, M., A. Tréhu, N. Cespedes, M. Kastner, U. Wortmann, J.-H. Kim, P. Long, A. Malinverno, J. W. Pohlman, M. Riedel, and T. Collett, 2008, Methane hydrate formation in turbidite sediments of northern Cascadia, IODP Expedition 311: Earth and Planetary Science Letters, **271**, 170–180, doi: 10.1016/j.epsl.2008.03.061.

Tucholke, B. E., G. M. Bryan, and J. I. Ewing, 1977, Gas-hydrate horizons detected in seismic-profiler data from the Western North Atlantic: AAPG Bulletin,

61, 698–707, doi: 10.1306/C1EA3DC5-16C9-11D7-8645000102C1865D.

Twichell, D. C., J. D. Chaytor, S. Uri, and B. Buczkowski, 2009, Morphology of late Quaternary submarine landslides along the US Atlantic continental margin: Marine Geology, **264**, 4–15, doi: 10.1016/j.margeo.2009.01.009.

VanderBeek, B. P., and A. W. Rempel, 2018, On the importance of advective versus diffusive transport in controlling the distribution of methane hydrate in heterogeneous marine sediments: Journal of Geophysical Research: Solid Earth, **123**, 5394–5411, doi: 10.1029/2017JB015298.

Walls, J. D., M. T. Taner, T. Guidish, G. Taylor, D. Dumas, and N. Derzhi, 1999, North Sea reservoir characterization using rock physics, seismic attributes, and neural networks; a case history: 69th Annual International Meeting, SEG, Expanded Abstracts, 1572–1575, doi: 10.1190/1.1820825.

West, B. P., S. R. May, J. E. Eastwood, and C. Rossen, 2002, Interactive seismic facies classification using textural and neural networks: The Leading Edge, **21**, 1042–1049, doi: 10.1190/1.1518444.

Wood, W. T., W. S. Holbrook, and H. Hoskins, 2000, In situ measurements of *P*-wave attenuation in the methane hydrate- and gas-bearing sediments of the Blake Ridge: Proceedings of the Ocean Drilling Program, Scientific Results, 164, Ocean Drilling Program, 265–272, doi: 10.2973/odp.proc.sr.164.246.2000.

Wrona, T., I. Pan, R. L. Gawthorpe, and H. Fossen, 2018, Seismic facies analysis using machine learning: Geophysics, **83**, no. 5, O83–O95, doi: 10.1190/geo2017-0595.1.

Xu, W., and C. Ruppel, 1999, Predicting the occurrence, distribution, and evolution of methane gas hydrate in porous marine sediments: Journal of Geophysical Research: Solid Earth, **104**, 5081–5095, doi: 10.1029/1998JB900092.

Yoo, D.-G., N. Kang, B. Yi, G. Kim, B.-J. Ryu, K. Lee, G. H. Lee, and M. Riedel, 2013, Occurrence and seismic characteristics of gas hydrate in the Ulleung Basin, East Sea: Marine and Petroleum Geology, **47**, 236–247, doi: 10.1016/j.marpetgeo.2013.07.001.

Biographies and photographs of the authors are not available.